# Continuation of Research in Seismic Techniques for Characterizing Levees

Richard D. Miller
Julian Ivanov
Shelby L. Walters

Kansas Geological Survey
1930 Constant Avenue
University of Kansas
Lawrence, Kansas 66047

First Report to

Joe Dunbar
U.S. Army Corps of Engineers – WES
3909 Halls Ferry Road
Vicksburg, MS 39180

Open-file Report No. 2006-48

June 2006

# Continuation of Research in Seismic Techniques for Characterizing Levees (first report)

## Line 1 Analysis

### *MASW*

### Optimizing Surface-wave analysis trace-offsets selection

To establish a general understanding of energy partitioning and model distribution we analyzed several representative shot records retaining all the traces. At this stage most effort was focused on observing the native dispersion curve trends (Figure 1a).

The quality of fundamental mode energy was appraised for six spread-offset ranges starting with the closest (6-60 ft), in which the fundamental mode and higher modes were blurred together (Figure 1b), and concluding with the long offset range 6-110 ft (Figure 1g). The range 6-100 ft offset range (Figure 1f) was selected to be optimal for picking the fundamental mode of the surface wave. Greater offset (Figure 1g) was avoided to allow for higher lateral resolution of the survey.

It was estimated that the levee was principally interrogated by frequencies above 25 Hz. The wavelength for 25 Hz energy was roughly estimated to be 450(ft/s)/25(Hz) =18 ft, which is a wavelength theorized to mainly represent materials in the upper 9ft (using half wavelength assumption). Furthermore at 60 Hz the fundamental mode is 350(ft/s)/60(Hz) =6 ft wavelength = 3ft depth. Therefore, frequencies above 60 Hz would primarily provide information for the upper 3 ft below the levee crest. Guided by the previous observations the selection of the optimum spread for analysis keyed on the fundamental mode energy around and above 25 Hz.

### Traditional MASW processing

Initially the dispersion curves were interpreted for all observed frequencies (6 to 80 Hz; Figure 2). The inversion results provided a 2-D Vs image for depths down to 60 ft (Figure 3). These results provided important guidance and information about the overall structure of the sediments as a function of depth but possessed little detail about the levees themselves, which was constrained to the top 10 ft of the section.

### Levee focused MASW processing

To better focus and control the MASW method on the levees themselves we edited the dispersion curves, removing frequency component estimates below 10 Hz. The lack of very low frequencies forced the software to use a shallow inversion model (max 26 ft deep). With this more depth-constrained model the inversion model focused on the shallower portion of the line (Figure 4) providing a much better image from within the levee.

## *Efforts to improve the levee imaging*

### *FDSE*

The FDSE filtering method (Park et al., 2002) was tested to evaluate its effectiveness in removing higher mode energy, which was interfering with fundamental mode. For these data it was especially difficult to apply FDSE due to the minimal separation in the velocity characteristics of the different surface-wave modes for the targeted frequency range (above 25 Hz to at lest 50 Hz).

### *Muting tests*

Muting selective energy (Ivanov et al., 2005) on representative records from Line 1 data showed great promise for improving the dispersion curve picking confidence in the 25-90 Hz range, thereby better imaging the levee (Figure 5). Conservative muting enhanced both fundamental and higher mode energy in the targeted frequency range of 25 - 50 Hz (Figures 5b and 5e). Thus, muting did not serve its primary purpose, namely the reduction and ideally the elimination (suppression) of higher-mode energy. Furthermore, more agressive muting preserved higher mode while the fundamental-mode energy may be barely traceable (Figures 5c and 5f). Three mute patterns were applied to all shot gathers from line 1 to provide dispersion curves that allowed better estimates of the fundamental mode.

We applied agressive muting to all the shot records, specifically muting all the dominant surface-wave energy. The remaining seismic energy of the seismic record was analyzed in search of fundamental-mode energy. Dispersion curves were picked (Figure 5b) from this editing in the t-x domain. Then the dispersion curves from the muted data set were combined with the unedited, full frequency range dispersion curves. The combined dispersion curves were inverted using a maximum depth model (Figure 6). The obtained Vs results are nearly identical to those from the inversion that used the initially picked dispersion curves (Figure 3). To better focus on the levee itself a shallower model (max 26 ft deep) was used to invert the combined dispersion curves (Figure 7). The later Vs results provided no improvement in imaging the levee compared to the Vs from unmuted dispersion curves using the shallow model (Figure 4). More subtle-muting results showed little improvements over inversions from muting and are not displayed.

## Reverse Line Processing

The MASW analysis on data with reverse shot-receiver orientation had weaker higher modes. Such a relative decrease of higher-mode energy allowed better fundamental and higher mode separation (especially between the targeted frequency range 25-50 Hz). This was accomplished by using a slightly longer spread length (110 ft [Figure 8] instead of the 100 ft, used for the Forward analysis). Such a benefit in mode separation actualized by using a longer spread was not observed on the forward data (Figures 1f and 1g). Furthermore, subtle muting (Figure 9b) enhanced the targeted 25-55 Hz range of the fundamental-mode dispersion curve (Figure 9d). For comparison, subtle muting was ineffective in enhancing the fundamental mode image on forward data from the same location (Figure 10).

At present, it is unclear why it was easier to observe and separate fundamental-mode energy from higher modes on reverse line data compared to the forward line.

### *Muting Processing of Reversed Line*

Non-aggressive muting applied to all the shot gathers from the reversed data set made the fundamental mode easier to pick within and below the desired frequency range of 25-50 Hz (12-14 Hz) (Figure 11). This allowed avoiding dispersion-curve combinations and running a shallower model (half space at 25 ft) inversion. The image resulting from this approach showed significantly better the top part of the levee (Figure 12).

### *P-wave First Arrivals*

First-arrival P-wave energy at each trace was picked automatically on shot gathers with only minimal manual adjustments, necessary to compensate for slight variation in waveform and random noise (Figures 13 and 14). There are two distinctively different apparent first-arrival velocity trends from trace to trace on the P-wave data (Figures 13 and 14). From the perspective of basic refraction analysis the two distinctly different phase velocities (approximately 950 ft/s and 5500 ft/s) observed in these data are likely from material within the levee and shallowest portion of the native earth (possibly the near-surface material [upper few feet of native sediments]). A 2-layer model solution (consistent with the two observed apparent slopes) places the depth of the high-velocity (5500 ft/s) refractor at about 18 ft. Refraction-tomography analysis provided a detailed 2-D Vp solution for line 1 (Figure 15). The 2-D solution represents a cross sectional slice of the levee, physically equivalent to cutting a slice parallel to the centerline (axis) of the levee, remaining one side, and observing the material cross-section from some distance away either north or south. This solution was obtained after minimal model iterations and provides an excellent match between the modeled and observed first arrivals. The 2-D Vp solution for line 1 was rescaled in both dimensions (x and z) to better focus on the levee and for ease of comparison with the rest of the results (Figure 16).

## Line 2 Analysis

### *MASW*

The fundamental-mode component of the surface-wave was strong enough that no additional filtering was required to estimate the dispersion curves within the targeted frequency range of 25-50 Hz (modeled to primarily sample levee material) (Figure 17).

### Traditional MASW processing

Following line 1 processing , dispersion curves were initially picked for all observed frequencies (6 to 80 Hz). The inversion results provided a 2-D Vs image to depths as deep as 60 ft (Figure 18). These results provided important information on the overall structure and lithology of the sediments within that depth range but possessed little detail from within the levees, represented by the top 10 ft of the section.

## Levee focused MASW processing

Consistent with the inversion analysis and methodologies used on line 1, dispersion curves were edited to remove frequencies below 14 Hz in an attempt to better focus the MASW method on the levees. An improved levee image was obtained by using the same shallow inversion model (max 26 ft deep) to obtain a 2-D Vs section (Figure 19).

### *P-wave First Arrivals*

First-arrivals on shot gathers on line 2 had the same characteristics as on line 1 and were picked automatically with only a very few needing manual adjustments. A refraction-tomography processing provided a detailed 2-D Vp solution for line 2 (Figure 20). For these data the 2-D solution represents a cross sectional slice of the levee, physically equivalent to cutting a slice from the levee parallel to the centerline (axis) of the levee. The solution was obtained with minimal model iterations providing an excellent match between the modeled and observed first arrivals. The 2-D Vp solution for line 2 was rescaled to focus on levee material and for ease of comparison with the rest of the results (Figure 21).

# Line 3 Analysis

### *MASW*

The fundamental-mode component of the surface-wave was strong enough to permit estimation of dispersion curves (similar to line 2) within the levee-targeted frequency range of 25-50 Hz without additional filtering (Figure 17).

## Traditional MASW processing

Consistent with the processing strategy of the previous lines, dispersion curves were initially picked for all possible frequencies (6 to 80 Hz). Inversion results provided a reasonable 2-D Vs image for depth range 2 to 60 ft (Figure 22). These results provided important general information of the overall structure and to some degree character of the sediments as a function of depth but unfortunately possessed little detail about the internal characteristic of the levees themselves, which were represented in the top 10 ft of the section.

## Levee focused MASW processing

Based on the findings resulting from the inversion analysis of line 1, we edited the dispersion curves and removed frequency estimates below 14 Hz to better focus the MASW method on the levees. The same shallow inversion model (max 26 ft deep) was used in obtaining a 2-D Vs section (Figure 23). Using this approach, it was possible to generate a better image of the levee.

### *P-wave First Arrivals*

Characteristics of first-arrivals from line 3 were consistent with the previous two lines and were picked automatically from shot gathers with the need for very few manual adjustments. The

refraction-tomography analysis provided a detailed 2-D Vp solution for line 3 (Figure 24). The 2-D cross section represents a property-specific view or slice of the earth vertically beneath the survey line. This solution was obtained with a minimal number of model iterations and provides an excellent match between the modeled and observed first arrivals. The 2-D Vp solution for line 3 was rescaled to focus on the levee and for ease of comparison with the results of other analysis (Figure 25).

## Observations

The levee body can be observed as a high Vs anomaly in the depth range 4-8 ft on all 2-D Vs images. Seismic data from lines 2 and 3 provided better fundamental-mode dispersion-curve images compared to line 1. This difference is likely related to levee homogeneity and corresponding backscatter noise. Such difference adversely affects the ease with which the MASW method can be used to provide equivalent side-wide comparison.

The levee image on line 3 is disturbed between locations 6100 – 6200 ft. From the pattern observed in the levee image patterns it can be proposed that part of the levee structure at this location is native materials consistent with those below the base of the levee (Figure 23). A similar high Vp anomaly can be observed at the same location on the corresponding refraction-tomography model of line 3 (Figure 25), which supports this interpretation. Of course there are many other possible interpretations but considering the settings this seems most reasonable.

## Ponding Experiment

One aspect of the work at this site is a continuation of an applied research project that was designed to evaluate the applicability of several seismic techniques to identify, delineate, and estimate the changes in physical characteristics or properties of materials within levees during a simulated flood event.

A pond, approximately 90 ft wide, was designed and built using earth material on the east side of a levee segment, which had experienced invasion from small mammals leaving burrows 0.07-0.10 m in diameter. The pond was gradually filled with water from the Rio Grande River at a rate that simulated modeled 100-year-flood conditions.

A line of compressional-wave geophones was deployed along the east edge of the levee road toward the pond and outside the area disturbed by pond construction. The pond mimicked the levee as closely as possible with the levee crest approximately 18 ft wide and 9 ft high with a 1-to-3 slope on each side. For the ponding experiment 10 Hz compressional-wave geophones were spaced at 2 ft apart. The total spread length was 240 ft requiring 120 recording channels.

Identical seismic data were acquired nine different times, at 4-hour intervals throughout the ponding experiment. Baseline data were acquired before the flooding test.

The water level gradually increased during the first 5 surveys and then varied (Figure 26).

## *P-wave First-Arrival Analysis*

Turning-ray tomography was used to define Vp for subsurface cells between the contact of the levee and native ground surface and the first 40 ft below the basal contact of the levee beneath the crest profile lines (Zhang and Toksoz, 1998).

## First-arrival picking

First-arrival seismic energy automatically picked off shot gathers required only minor manual adjustments (Figure 27).

On many shot gathers at source-receiver offsets of ±40 ft first arrivals begin interfering with the air wave and as a result error in picking increases and confidence levels drop. A first pass at first-arrival picking was performed and a refraction-tomography solution was estimated with the knowledge that first-arrivals around 40 ft offset from the source were contaminated. Observed and modeled first-arrival times were then examined for inconsistent misfits with appropriate adjustments made.

Large positive (observed first arrivals are greater than the modeled) misfits between 2120 and 2180 (Figure 28) are noticed on only two of the shots. One possible explanation was that these misfits were result of inaccurate first-arrival picks due to noise. Another possibility was these positive misfits are result of a near-surface velocity anomaly within the levee. The first-arrival energy was reexamined again on raw shot gathers and alternative, weak first-arrivals, initially interpreted as noise, were estimated (Figure 29). The newly picked first arrivals matched well the calculated first arrivals from the initially estimated velocity model. In such a manner a first-pass refraction-tomography solution was used to identify which first-arrival patterns are due to noise and which are due to seismic response of the site. The newly interpreted first-arrival pattern could be observed on shot gathers at the same location from the following surveys during the ponding experiment.

The similar approach was applied on few of the negative misfits between 2090 and 2140.

Further examination of first-arrival misfits on traces within 60 ft of the source revealed negative misfits at some shots were balanced at the same stations by positive first-arrival misfits (from other shots). This variability occurs at the transition or cross-over between the first and the second apparent-velocity slopes. The negative misfits is the result of signal contaminated by the air wave in the transition zone. This transition zone was deliberately avoided during the picks, by selecting the wavelets appearing immediately after the air-wave signature. It was hypothesized that it is very likely within this zone the first arrivals interfered with the air wave, which could be supported by observations of stronger air-wave wavelets. Stronger air-wave wavelets supported by model estimated first-arrival times were used as a guide to pick first arrivals, which followed the air-wave trend for several traces.

The modeling and first-arrival pattern analysis was iterated four times to optimize the solution. Using that sequence the harmful influence of ambient noise and air wave of first-arrival analysis was minimized.

## *Choosing smoothing parameters and nonuniqueness.*

Choosing maximum smoothing constraints is widely accepted as the optimum approach when solving the inverse refraction-tomography problem (as well as any other ill-posed geophysical problem [Constable et al, 1987]). However, smoothing diminishes or eliminates local anomalies. Thus, such an approach may be very harmful when trying to detect or delineate local near-surface anomalies. When investigating levees, detail and delineation of anomalies is, generally, the objective. For this study, detail critical to describing the levee is evident in refraction-tomography solutions for line 1 (Figure 30).

One of the main criteria for finding a reasonable or best solution to the inverse refraction-tomography problem is the minimizing RMS error between the modeled and observed first-arrivals. Rays that sample the near-surface arrive at near offsets, and rays that sample the deeper parts of the section arrive at far offsets. In addition to the traditional RMS estimate we calculated the RMS fit between the modeled and observed first-arrivals for the very near-offsets (say, 20%), which is one of the measures developed for better understanding the focusing of the refraction-tomography analysis on the near surface.

Selecting regularization parameters (such as smoothing constrains) is considered subjective (Claerboat, 1992, p. 82), regardless of the algorithm used (Tichonov and Arsenin, 1977; Hansen, 1998; Xia et. al., 2005). No matter of its forms, *smoothing* quantifies expectations (about the solution), which are not based on actual data (Menke, 1989, p. 48). For this particular data set, we tested several degrees of smoothing, observing both total and near-offset RMS error and evaluating the solutions with the *a priori* information about the site and the MASW results.

We display three refraction-tomography solutions (Figure 30) using different smoothing weights. The weights stabilized the inverse problem by affecting second-order smoothing constraints. The applied weights were 150, 50, and 15 ((Figures 30a, 30b, and 30d), in both vertical and horizontal direction. Commercial refraction-tomography algorithms (Rayfract, GeoTomo, Green Mountain, etc.) would automatically select a smoother solution with smoothing parameter of 150 or higher (depending on their internal algorithm). This approach may be acceptable when estimating the near-surface model for static corrections but is inappropriate for the levee surveys because high smoothing smears or suppresses local anomalies. To chose which of the weights provides the most realistic solution we used Vs section from MASW analysis as additional *a priori* information. The refraction-tomography solution, which used a weight value equal to 50, was selected to minimize the resemblance with the Vs section between horizontal locations 2140 and 2160 and depths 8-10 ft (Figure 30b and 30d). The overall RMS error (1.22 ms) was equivalent to the near-offset RMS error (1.24 ms). The weighted (15) refraction-tomography solution showed improved near-offset RMS error (1.08 ms), implying a better fit for the near-surface rays paths. However, from a qualitative perspective this solution was too irregular to be considered realistic. Rejecting this solution was also supported by the available *a priori* geologic information, as well as from the MASW Vs images suggesting the base of the levee was flat. The maximum-smoothness solution had the overall RMS error (1.19 ms) but its near-offset RMS error was too big (1.38 ms), indicating poor near-surface representation of the Vp model.

## *Vp Models During the Ponding experiment*

Using the selected smoothing inversion parameters and first-arrival estimates nine Vp refraction-tomography models were estimated for each time slice during the ponding experiment (Figures 31 and 32).

The base line survey revealed a high-velocity Vp anomaly at the burrowed area observed between locations 2120 and 2160 ft (Figure 31, top section). This anomaly reached 10 ft depth at the start of the flooding experiment and after the first 4 hours could still be observed only at the very top 3-4 ft of the levee. Refraction-tomography Vp results for the rest of the line suggest compressional-wave velocity is not sensitive to the material changes that occurred in this segment attributed to the ponding (Figures 31 and 32). It is also possible that the levee surface sealed and no saturation occurred and due to that no material changes took place.

## *MASW*

The potential of the MASW technique to estimate the dispersion curve of the fundamental mode of the Rayleigh wave from compressional-wave data recorded on the levee crest was evaluated (Figure 33). The fundamental mode of the surface-wave energy was poorly defined compared to the first trip (Figure 2).

At the time of the ponding experiment the fundamental mode of the surface wave was well defined within a narrow frequency range 5-18 Hz and difficult to interpret at higher frequencies, especially above 30 Hz. As a result, Vs estimates for the top 5 ft of the levee have less confidence and need to be used with caution.

A baseline MASW survey was designed to establish an initial 2-D Vs section used as a reference (Figure 34, top section). Two anomalous high-velocity zones can be observed within the levee body at a depth of about 6 ft between locations 2095 and 2103 ft, and 2145 and 2165 ft. At time slices 2 and 3 (Figure 34, 2nd and 3rd sections from the top), representing 4 and 8 hours after the start of the water fill, the shear-wave properties change and the high-velocity anomalies begin to suppress. As the flooding simulation continues at time slices 3, 4, and 5 (corresponding image numbers from top of Figure 34) the Vs values within the levee continue to decrease to about 10-15 % their original values. At the same time a new low-velocity zone begins to form between locations 2098 and 2110 ft. This trend continues during time slices 6 and 7 (Figure 35), and by time slices 8 and 9 the low-velocity anomaly is well established and clearly representative of a change in the levee. Most likely this anomaly is consistent with ground water movement under the levee. Such water movement could be responsible for subsurface erosion, indicative of an area susceptible to weakening the levee subgrade. Extreme cases with prolonged high-water conditions and these anomalies could be susceptible to failure. Observation of such anomalies meets one of the objectives of the survey, which is to detect old streambeds running under the levees that could provide conduits for increased ground-water flow thereby indicative of weak spots more prone to failure during flooding.

## Discussion

Comparing the Vp and Vs estimates between the two trips shows that, at the time of trip 2, there is a general decrease of Vs (Figures 36) and at least 15 % increase of Vp (Figures 37) within the levee (top 10 ft) compared to trip 1. Vp velocity increase between 15 and 20% is evident for most of the top 10 ft; with the exception of the 2110-2160 ft offset range, where the velocity decreases above 40%.

Therefore, during trip 2 the Vp/Vs ratio (Poisson's ratio) is higher during trip 1. High Vp/Vs ratio can produce strong higher modes and weak fundamental mode (Park, personal communications) as observed during the second trip. This observation is important for the overall understanding of the ease of the applicability of the MASW method. It was relatively easy to estimate the fundamental mode of the surface wave during the first trip, while it was very challenging to evaluate it during the second trip.

## Conclusions

Shear-wave velocity calculated from surface-wave energy using the MASW method appears to have changed as a result of the ponding experiment. We assumed these seismic changes are in response to increased saturation below the levee caused by water infiltration during the flood simulation. No noticeable changes occurred in the compressional-wave properties of the levee material except for a small area within the levee speculated to be affected by burrowing. Vs was the property measured to be most significantly affected by the presence of ponded water.

In general, both compressional- and shear-wave velocity estimates for this type of silty sand levee suggest changes due to high water conditions might lead to lower Vp and Vs values and thus decrease levee strength.

## P-wave Reflection Seismic Next to the Pond

The objective of the experiment was to monitor change in the shallow water table based on changes in seismic reflectivity due to changes in density or velocity as sediment saturation increased. It was of interest to note whether or not this change was uniform. Since the line was shot multiple times, it was of interest to determine what effect, if any, the source had on the results. Specifically, change in source signature may account for variation from one run to the next, which would have to be accounted for during data processing in order to compare the stacked sections from one run to another.

A seismic reflection line ran parallel to the levee in the floodplain between the river and the dam approximately 20 feet from the base of the dam, extending nearly its entire length. Two 40 Hz geophones with 1 foot spacing were used. There were 2000 samples per trace with a 0.25 ms sample interval. The source was a 30.06 fired down hole; source spacing was 8 feet. A baseline survey was shot first, after which water was pumped into the pond for 4 hours.

## Seismic reflection processing

The first run was processed using the procedure described below; the remaining 8 runs were processed the same, except for velocity analysis. Normal move-out was corrected for each run individually.

Automatic gain control (AGC) with a 20 ms window was applied in order to amplify the raw data. The field geometry was then assigned. The data were filtered with a bandpass filter of from 100 to 500 Hz. Bad traces were muted. Static corrections were then made based upon GPS elevation data. First arrivals, surface waves, and air waves were filtered using a filter in the frequency-wave number domain. This technique was successful at suppressing the air waves and enhancing signal, but the remaining portion of the air waves was surgically muted along with everything except usable signal. The data were then resorted into CMPs. Velocity analysis was done, the data were corrected for normal move-out, and stacked in order to produce a final stacked section.

Note that spectral balancing and spherical divergence corrections were both attempted. Spectral balancing greatly decreased the amplitude of the data. Correcting for spherical divergence made no significant difference in the quality of the data. Therefore, neither of these processing techniques were used to produce the final stacked sections.

After processing, the data were reprocessed using the procedure described above, except for the AGC. This was done to preserve true amplitudes for analytical purposes.

## Seismic reflection analysis

Immediately during processing was the strength of the air wave. Qualitatively, its strength appeared to drop from the first run to the second, then strengthen throughout the remaining runs. In order to analyze its strength as it changed with time, everything except the air wave was muted from the shot gathers after the bandpass filter was applied. The frequency spectra were found for each shot gather of each run. There were several different peak frequencies in the air wave. The true amplitudes of these peak frequencies were recorded from each frequency spectra. The average amplitude of each frequency was calculated for each run and plotted as a function of time. The average amplitude of the air wave was found by averaging the mean amplitude of each frequency for each run and plotted as a function of time (Figure 38).

The remaining signal and noise after surgically muting undesired data was then analyzed in the same fashion as the air wave (Figure 39).

In order to understand how reflection strengths changed, the same trace in the same shot gather was analyzed for each run. Everything except the desired reflection was surgically muted from the first four shot gathers, and a frequency spectrum for each of these shot gather was generated. The peak frequency and its amplitude were recorded, and two plots were generated for each shot gather: the reflection frequency vs. time, and reflection amplitude vs. time. This was done for the reflections at approximately 35.8 ms and 55.0 ms. The reflection frequency did not change significantly or with any sort of pattern. The reflection amplitudes vs. time can be seen for the 55.0 ms reflection in Figure 39.

In order to determine how the source signature changed with repeated shots, a single trace from the same shot gather during each run was selected. The correlation coefficient was determined for each of the nine wavelets, first correlated with the first wavelet, then with the second wavelet. This was repeated for 5 traces, both near and far from the source. Plots of correlation coefficient vs. time were generated for each, seen in Figures 40 and 41.

## Analysis of the Results

In Figure 38, note the distinct drop in amplitude from 14,064.29 units to 5784.217 between runs 1 and 2, a decrease of 59%. The average amplitude then increases nearly linearly throughout the remaining runs. The drop in air-wave amplitude between the first two runs is very significant. This shows that the source was coupling with the ground much better after firing the gun downhole once. Source coupling then linearly increases throughout the remaining seven runs. This suggests that, in order to optimize data acquisition in this setting using a 30.06 or similar source, one should fire a shot downhole before acquiring any data. This will allow for greater source coupling for successive shots fired. No more than eight shots can be fired before source coupling has degraded to what it was at the first initial shot.

In Figure 39, there is a drop in reflection amplitude between the first and second run, followed by a steady amplitude until it drops again between runs 8 and 9. The first drop is, on average, 38%. The second major drop is 60%, on average. Note that these amplitudes are not on the order of those of the air wave; these amplitudes are much smaller. This seems to indicate a level of consistency between runs 2 through 8, while there is a distinct change after 1 and before 9. Like it was determined from air wave data, reflection amplitudes also seem to indicate that optimal data acquisition is between runs 2 through 8 (though for different reasons).

There are three things to note about Figures 40 and 41. First is that the wavelets from other runs correlate much better with the wavelet from run two (Figure 41) than run one (Figure 40). Second, in general, the farther the geophone is from the source, the smaller the correlation coefficient. Third, the coefficients decrease through run 5, and then unexpectedly increase for the remaining runs.

The fact that the second run correlates better with successive runs than the first run indicates that there was a dramatic change in the source signature after the gun was fired downhole just once. Source signature does continue to change, but it is much more similar to the second run than the first.

It makes sense that the farther the geophone is from the source, the correlation is not quite as good. The energy has been transported farther and had more opportunity to distort (possibly due to slight changes in wave front due to small local variations in density and/or velocity).

The decrease in correlation coefficient with run is expected because of the change in source signature due to degradation of the hole and compaction of the surrounding unconsolidated sediments. This should be expected throughout the nine runs. However, there is a slight increase at run 6 and a significant increase at run 7. This does not correspond to any other significant change

at run 7. Therefore, there was some change that occurred that did not significantly affect any reflection or air-wave amplitudes and/or frequencies or seismic velocities.

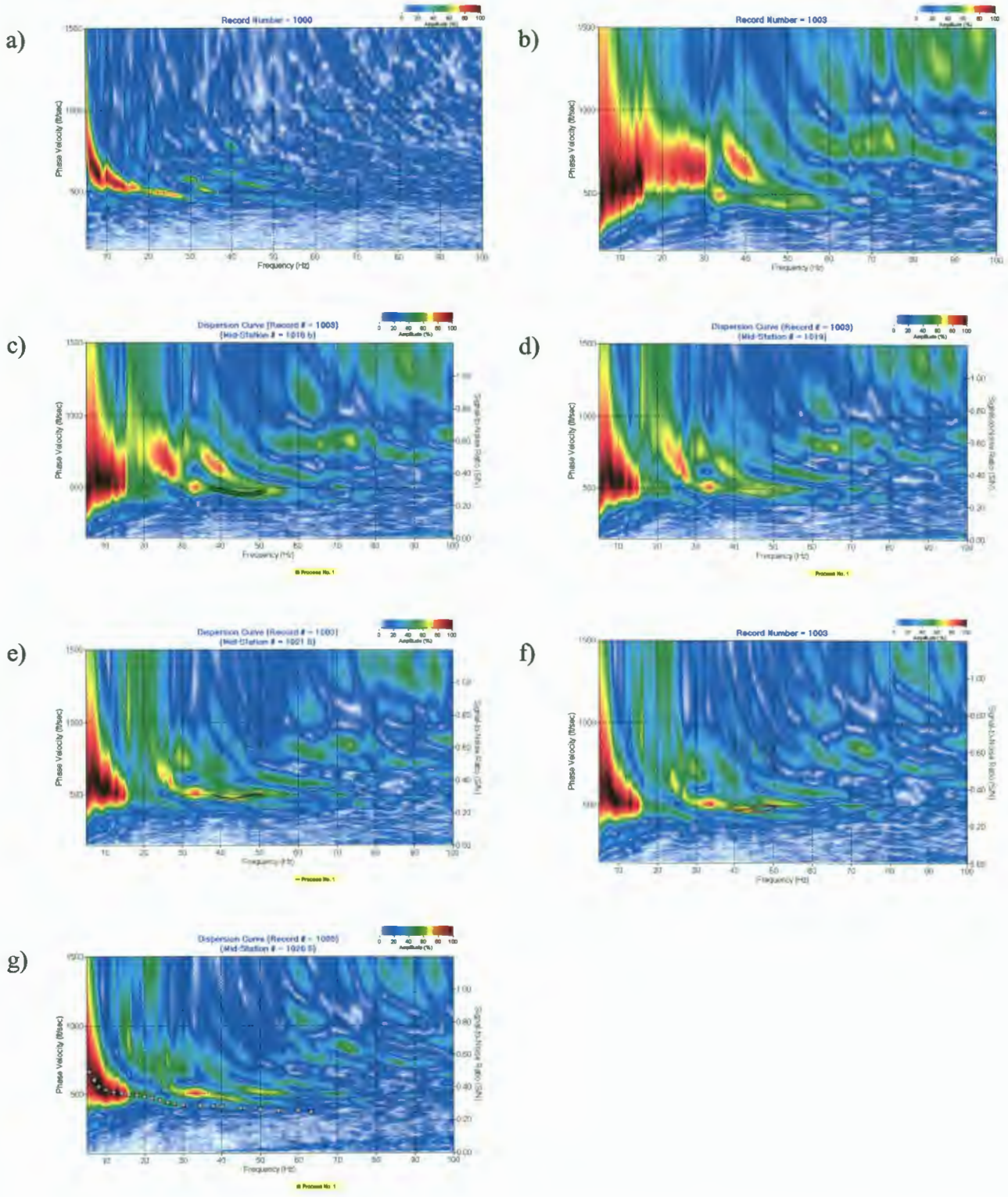
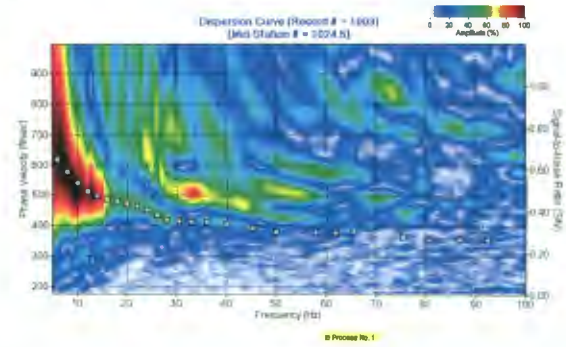
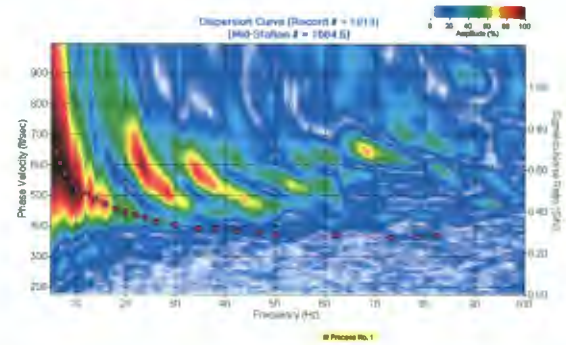



Figure 1. Phase-velocity – frequency transform of selected trace-offset ranges, a) all traces, b) 6 to 60 ft, c) 6 to 70 ft, d) 6 to 80 ft, e) 6 to 90 ft, f) 6 to 100 ft, g) 6 to 110 ft.

a)



b)



c)

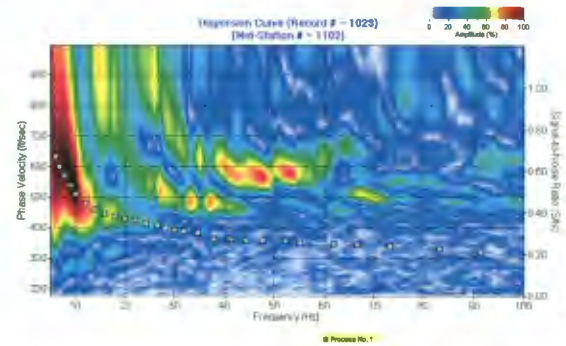


Figure 2. Line 1. Dispersion curve images extracted from the shot gathers located at the a) west end, b) middle, and c) east end of the line.

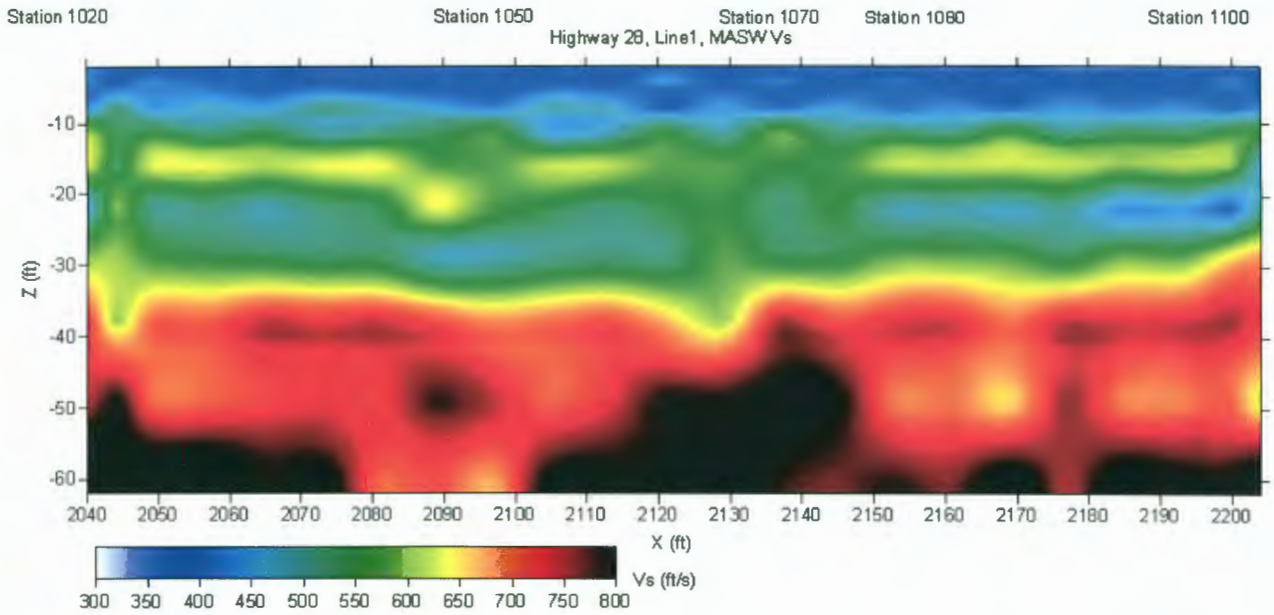



Figure 3. MASW Vs results for Line 1.

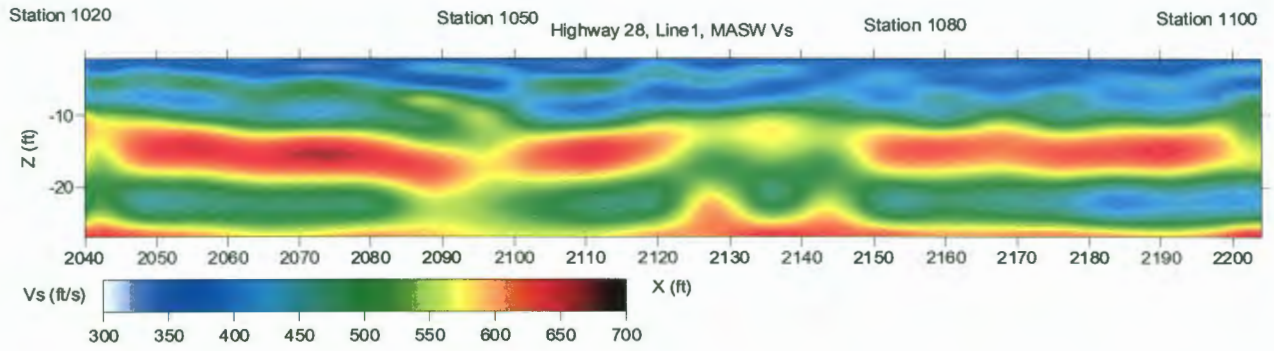



Figure 4. Shallow-focused MASW Vs results for Line 1.

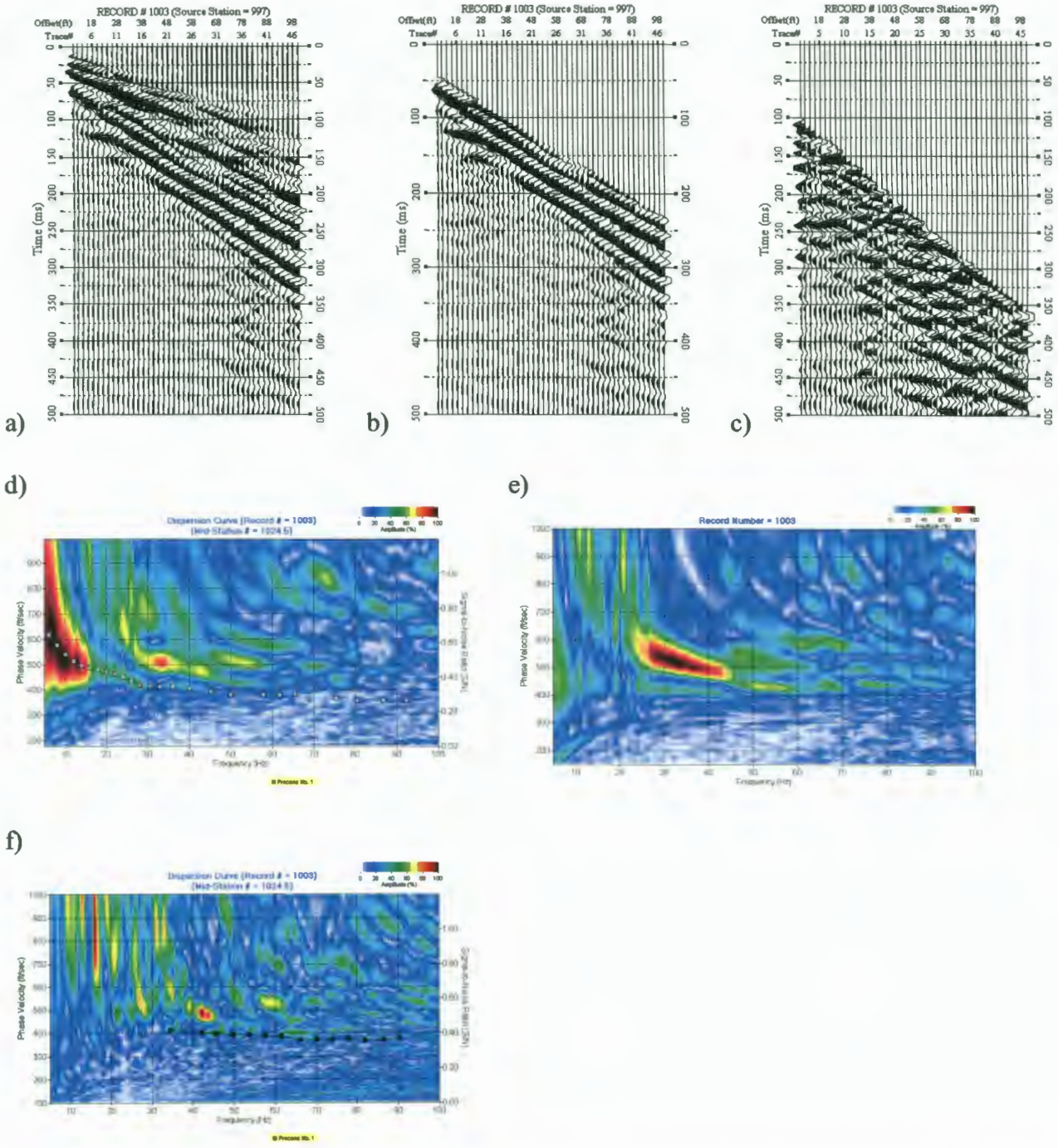



Figure 5. Testing muting on raw shot gathers of Line 1 to improve the dispersion curve imaging of the fundamental mode of the Rayleigh wave, a) raw shot gather, b) moderately muted higher mode c) strongly muted higher mode, and their corresponding phase-velocity – frequency images d), e), and f).

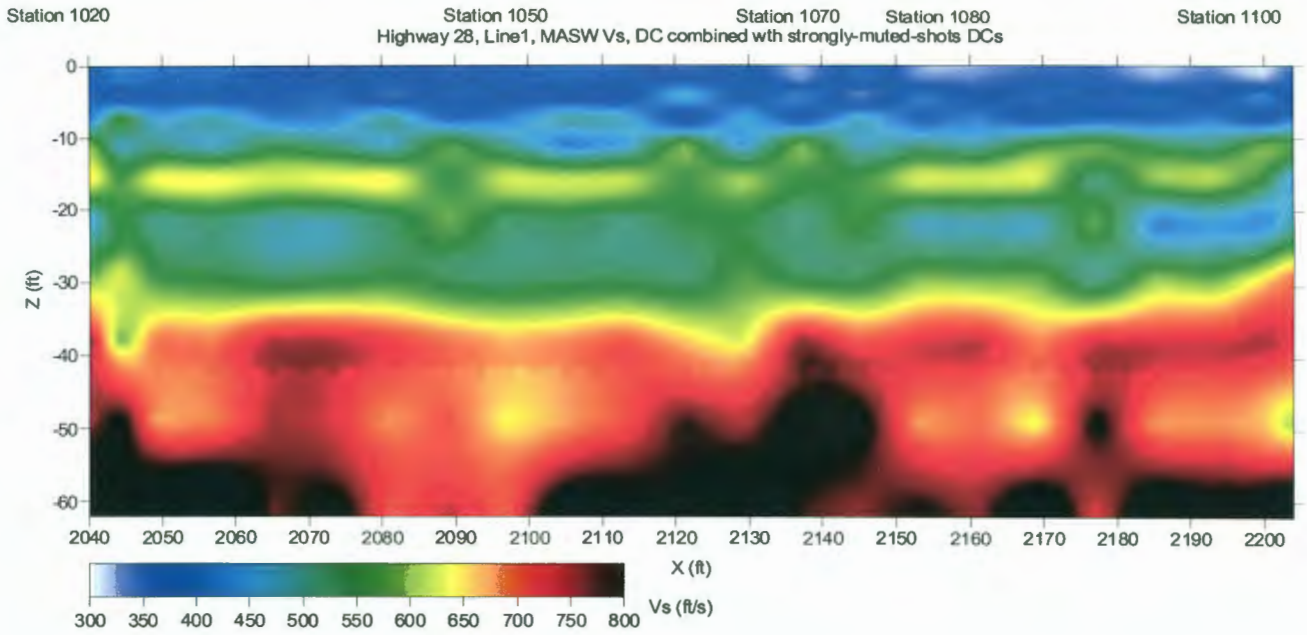



Figure 6. Line 1 MASW Vs results from combined dispersion curves, the higher frequency portions of which were estimated from the strongly muted data.

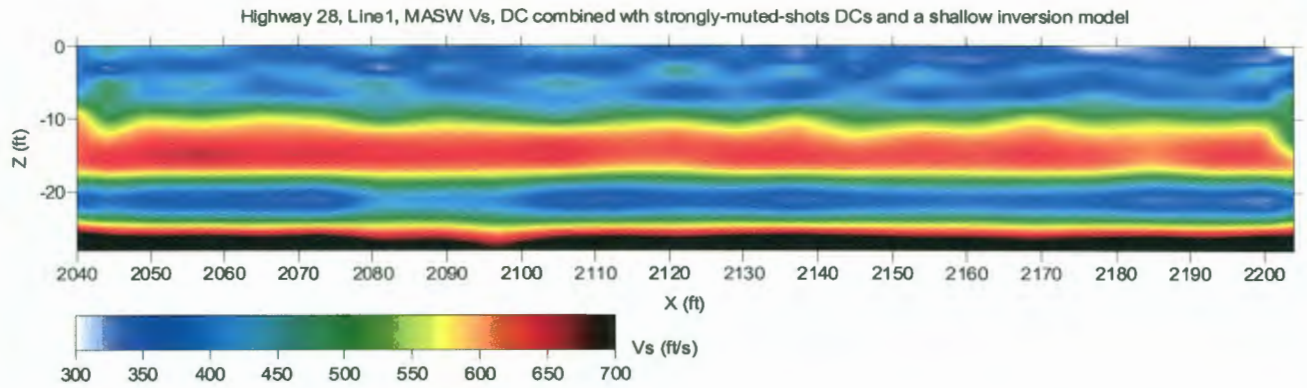



Figure 7. Line 1 shallow-focused MASW Vs results from combined dispersion curves, the higher frequency portions of which were estimated from the strongly muted data.

a) b)

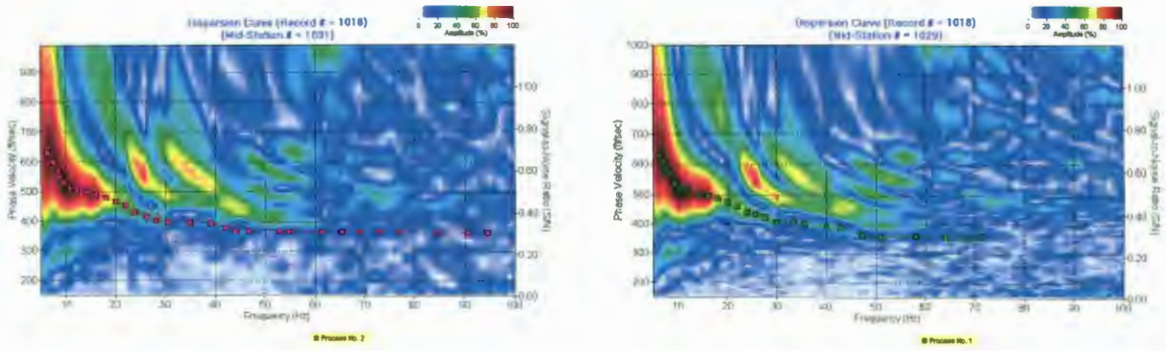
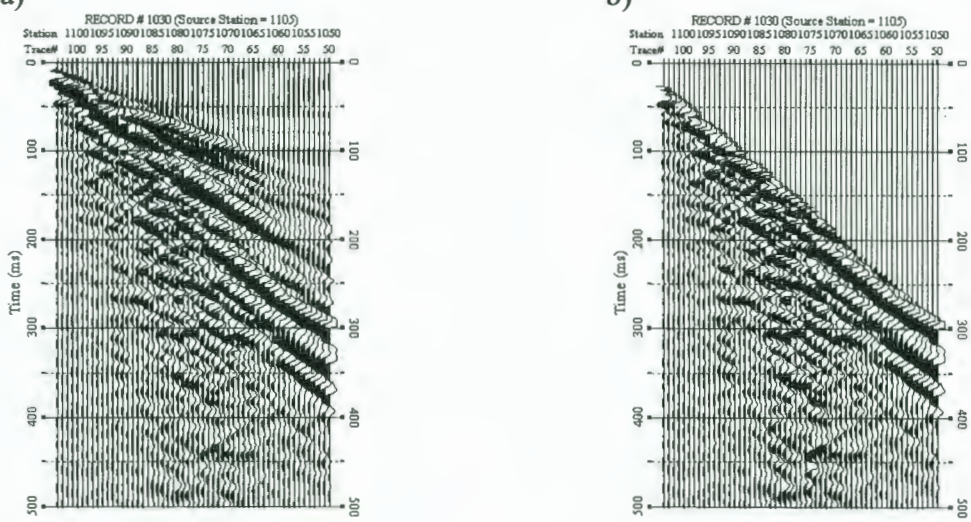


Figure 8. Line 1 reverse data. Phase-velocity – frequency transform of selected trace-offset ranges, a) 6 to 100 ft, b) 6 to 110 ft.

a) b)




c) d)

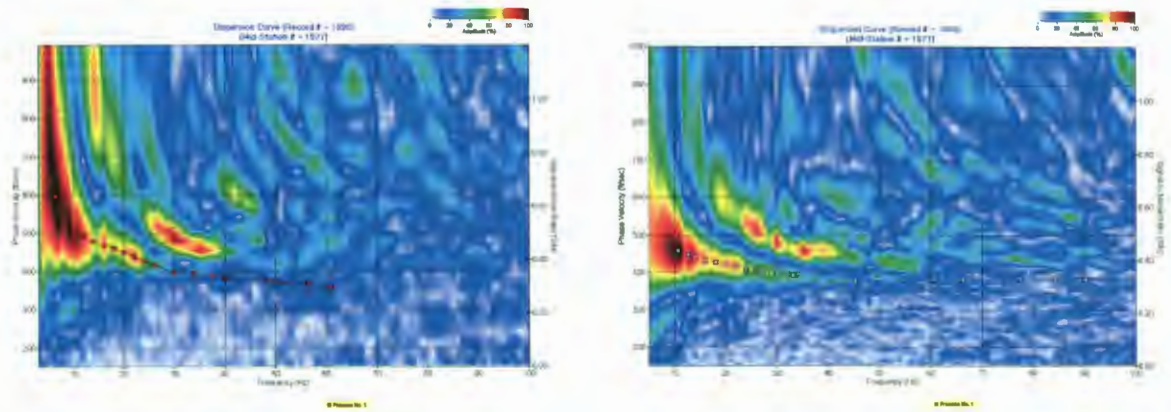


Figure 9. Line 1 reverse data. Mild muting b) on raw data a) improved the fundamental-mode energy between 25-55 Hz d) compared to the image of unmuted data c).

a) b)

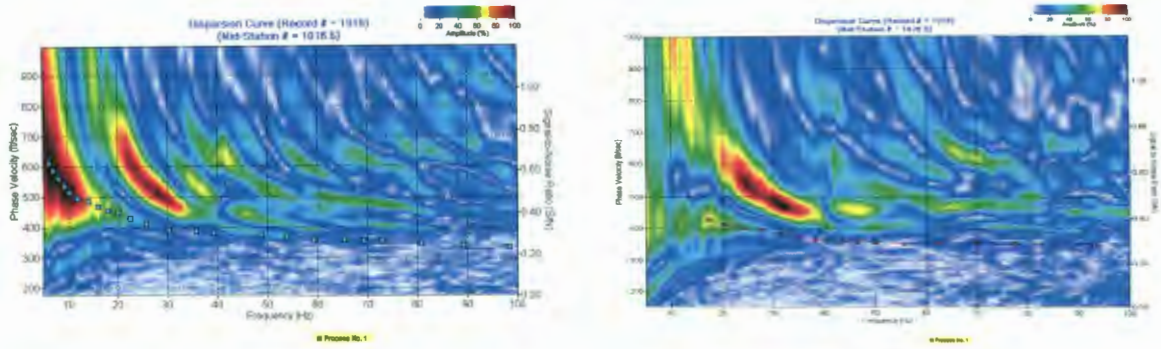
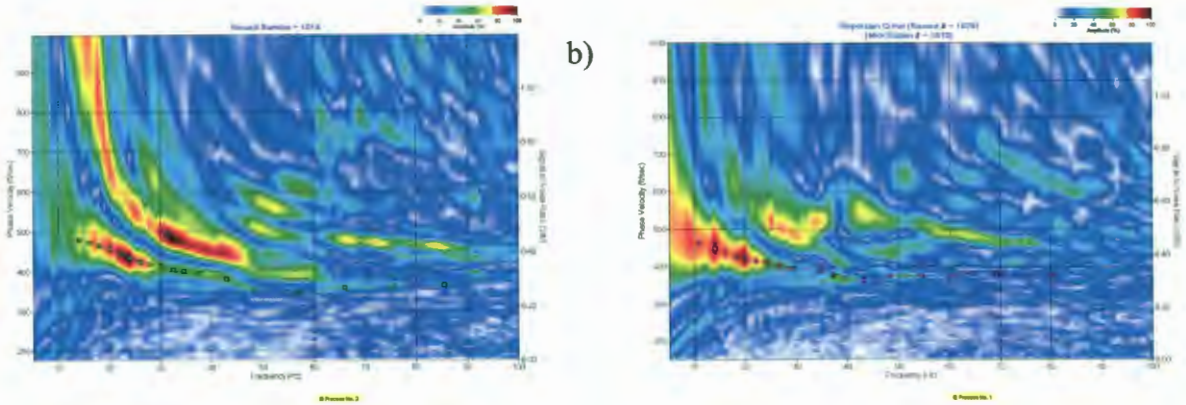


Figure 10. Line 1 forward data. Mild muting b) on raw data a) did not improve the fundamental-mode energy between 25-55 Hz d) compared to the image of unmuted data c).

a) b)



c)

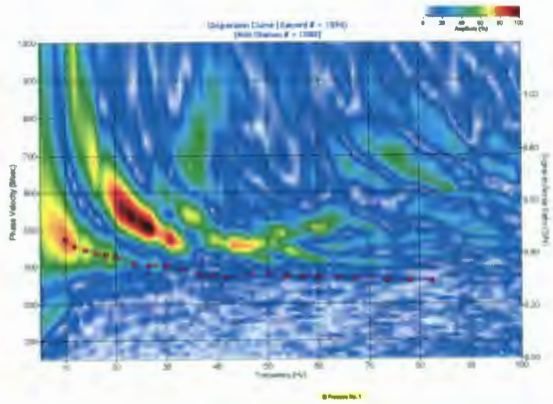


Figure 11. Line 1 reverse data. Dispersion curve images extracted from the mildly muted shot gathers located at the a) west end, b) middle, and c) east end of the line.

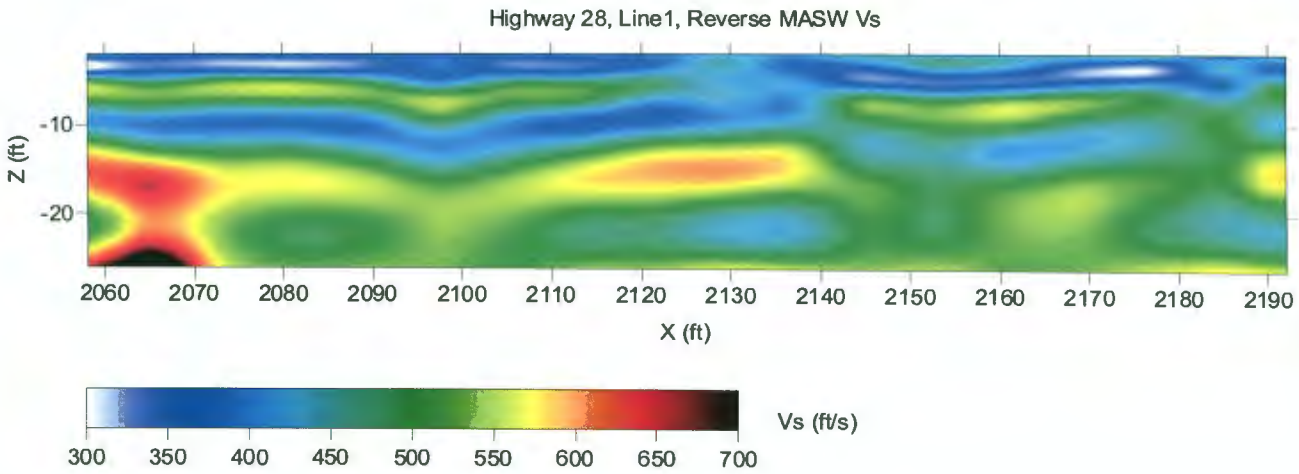



Figure 12. Line 1 reverse data MASW Vs results.

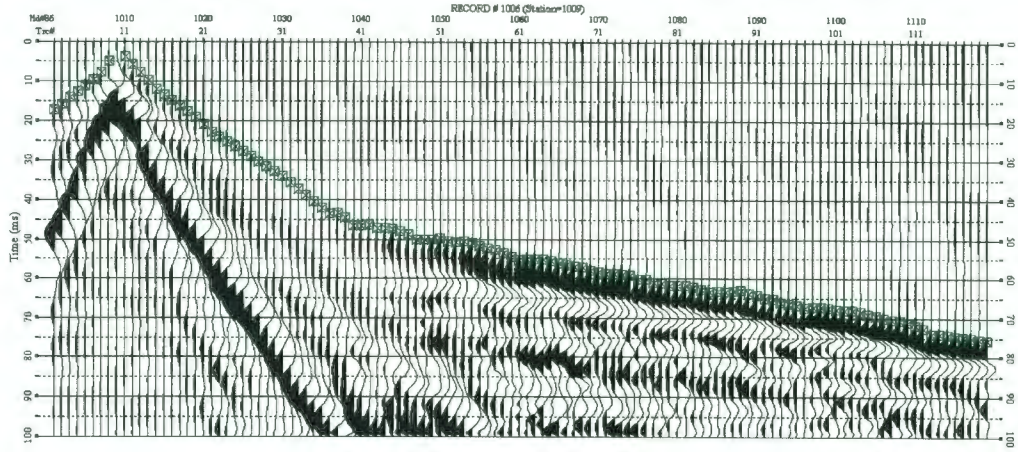


Figure 13. Estimation of first-arrival times on a P-wave seismic data with source located at station 1009 (horizontal location 2018 ft).

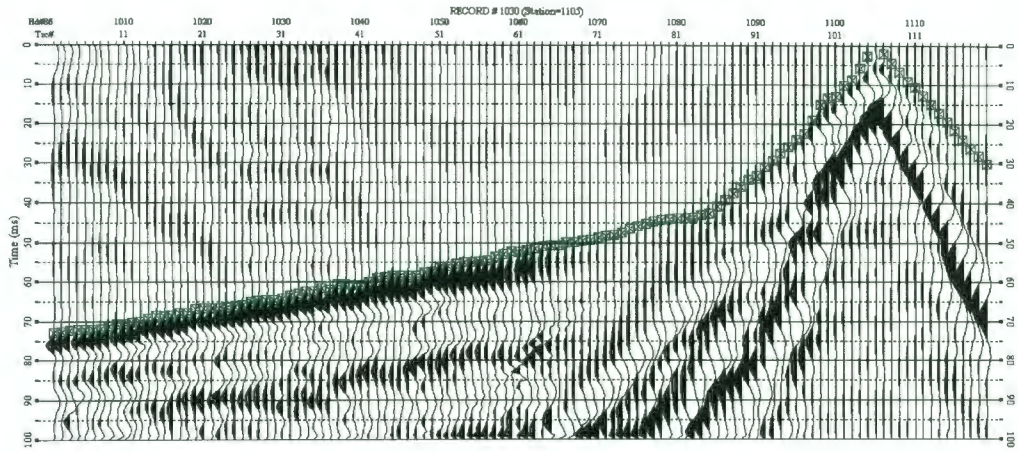


Figure 14. Estimation of first-arrival times on a P-wave seismic data with source located at station 1105 (horizontal location 2210 ft).

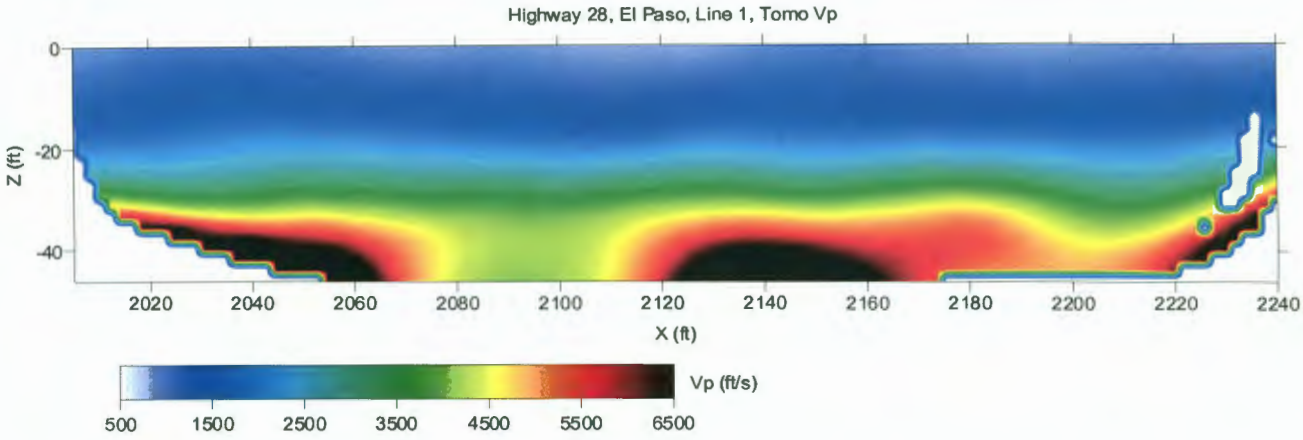



Figure 15. P-wave velocity model estimated for line 1 by analyzing P-wave-data first-arrival times using refraction-tomography software.

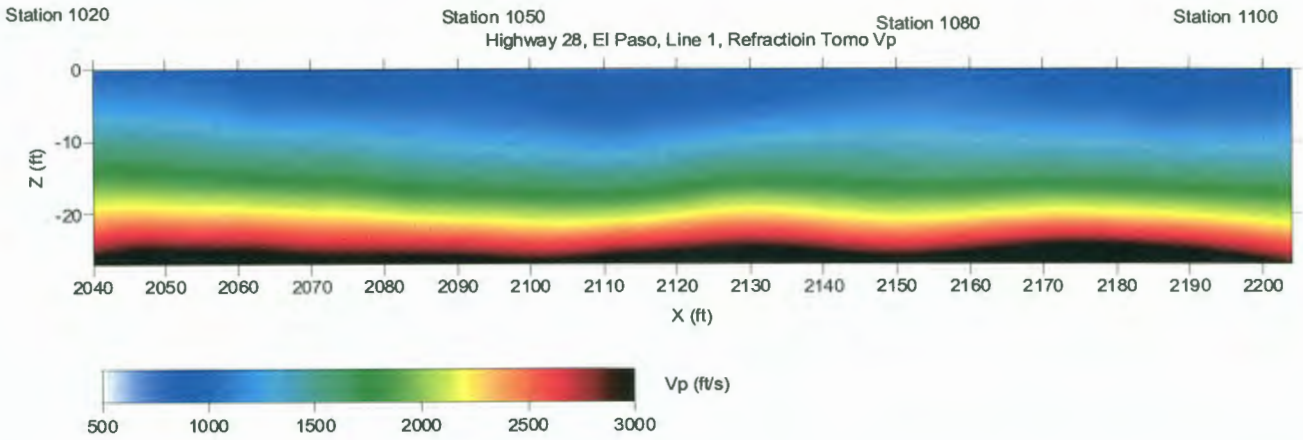



Figure 16. P-wave velocity model estimated for line 1 by analyzing P-wave-data first-arrival times using refraction-tomography software rescaled for comparison with the rest of the Vp and Vs results focusing on the levee.

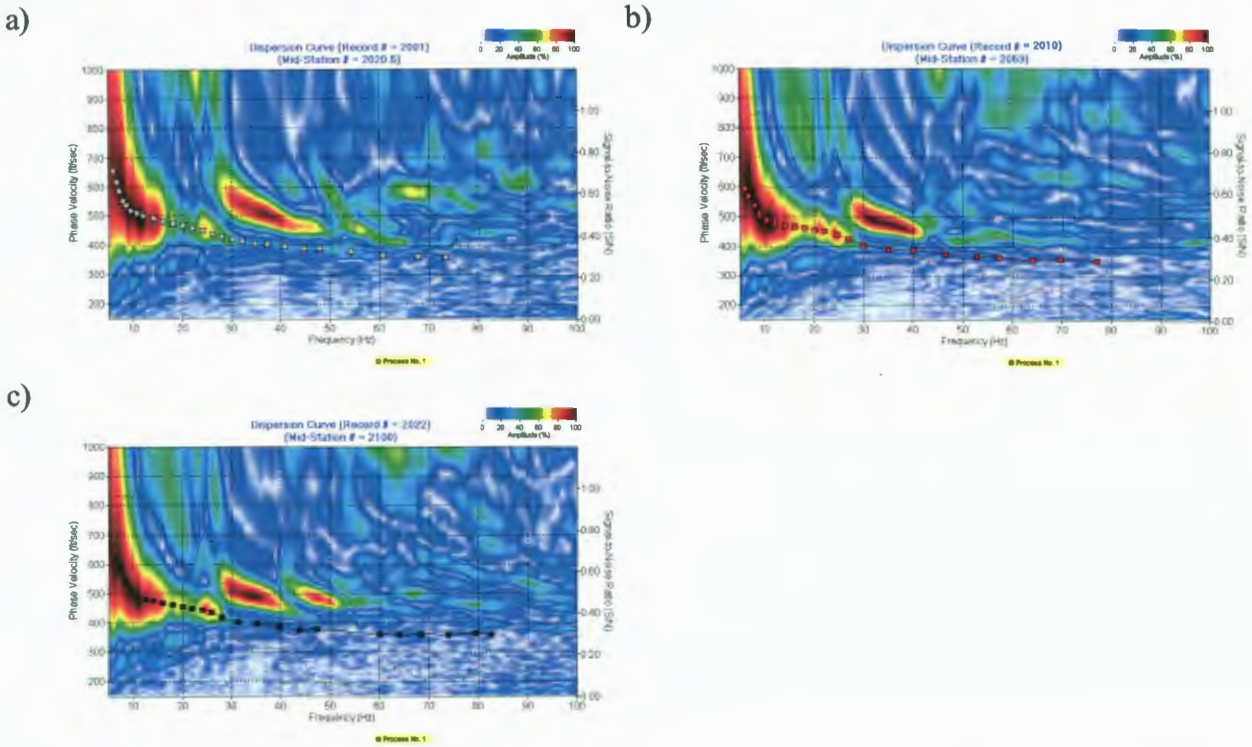



Figure 17. Line 2. Dispersion curve images extracted from the shot gathers located at the a) west end, b) middle, and c) east end of the line.

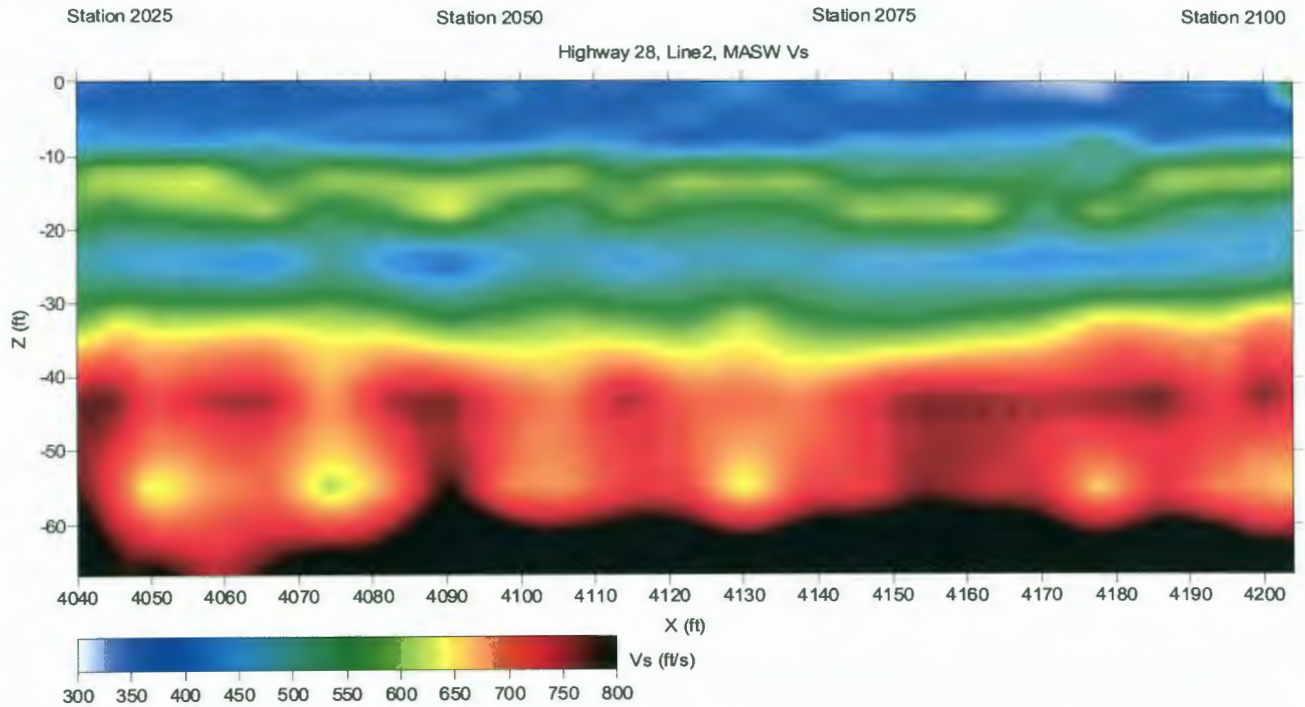



Figure 18. MASW Vs results for Line 2.

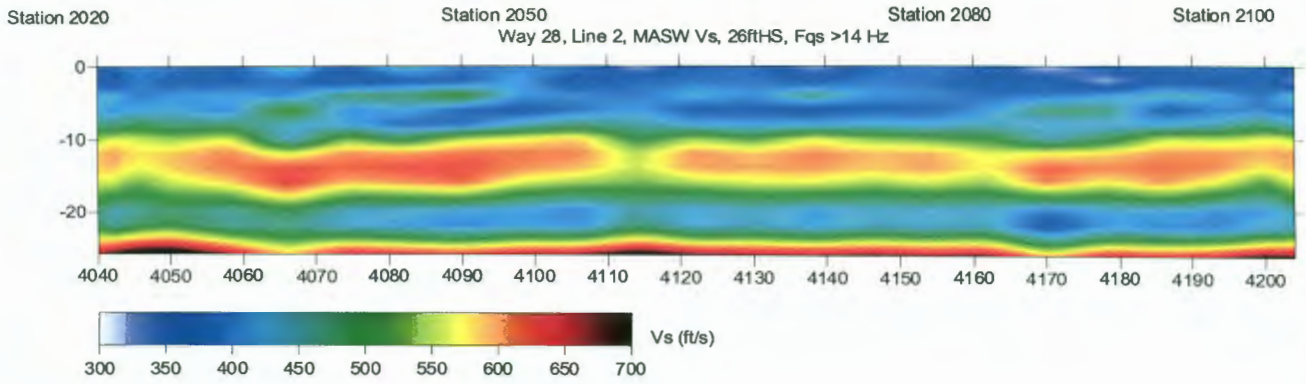



Figure 19. Shallow-focused MASW Vs results for Line 2.

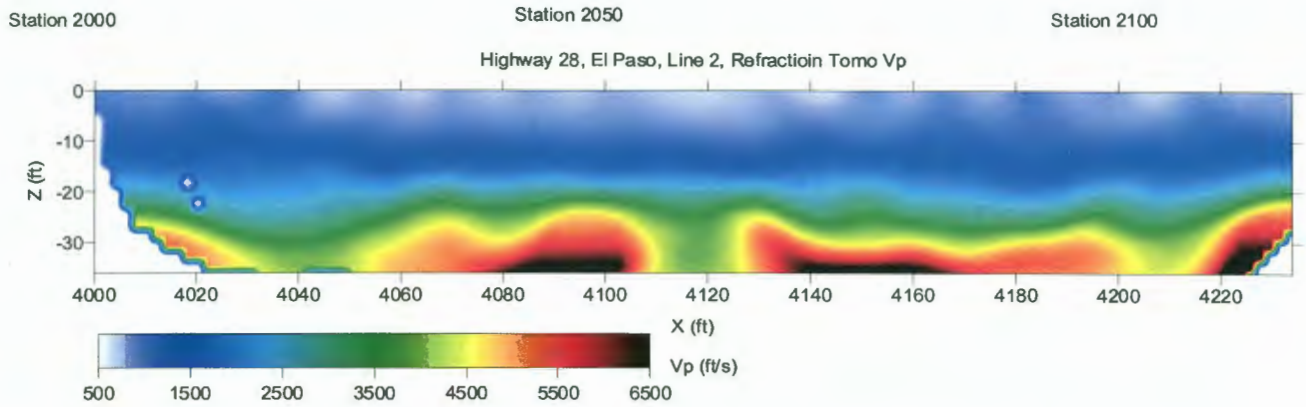



Figure 20. P-wave velocity model estimated for line 2 by analyzing P-wave-data first-arrival times using refraction-tomography software.

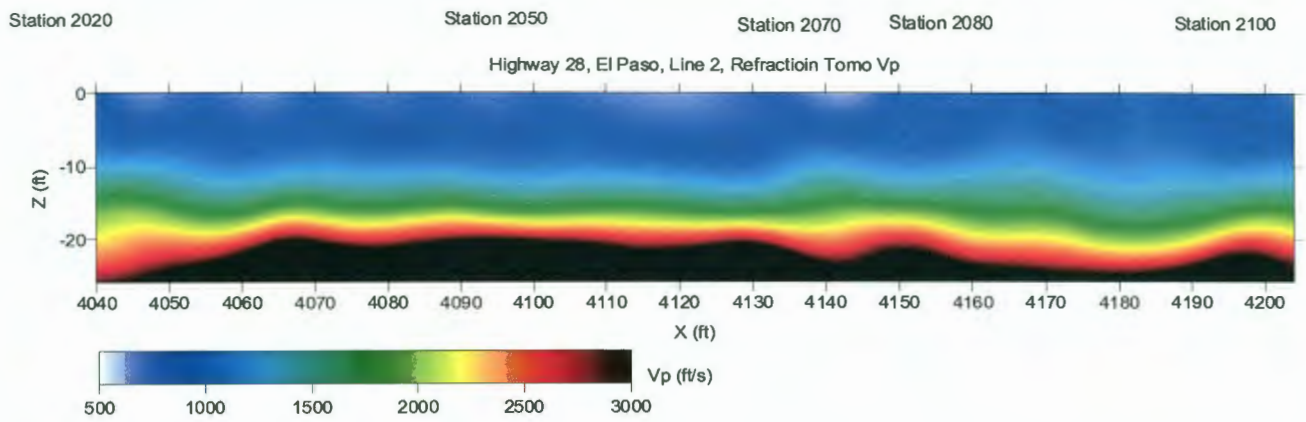



Figure 21. P-wave velocity model estimated for line 2 by analyzing P-wave-data first-arrival times using refraction-tomography software rescaled for comparison with the rest of the Vp and Vs results, focusing on the levee.

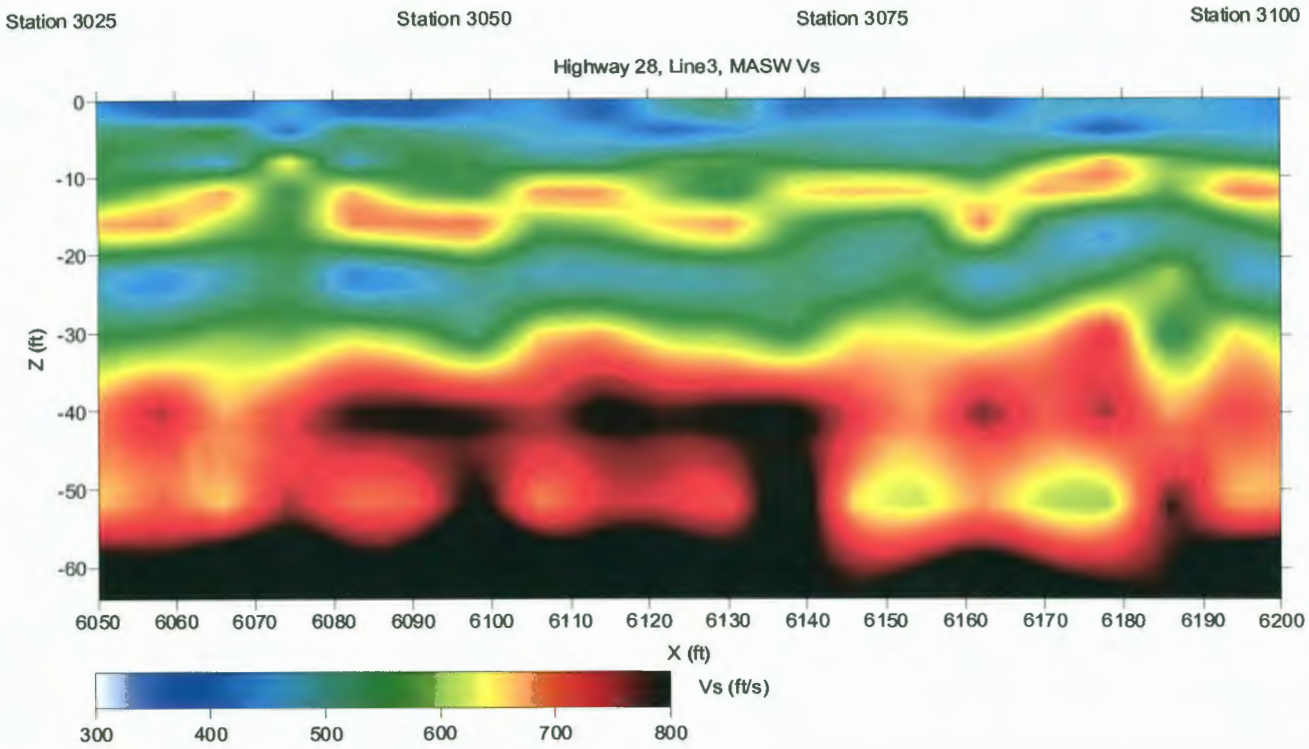



Figure 22. MASW Vs results for Line 3.

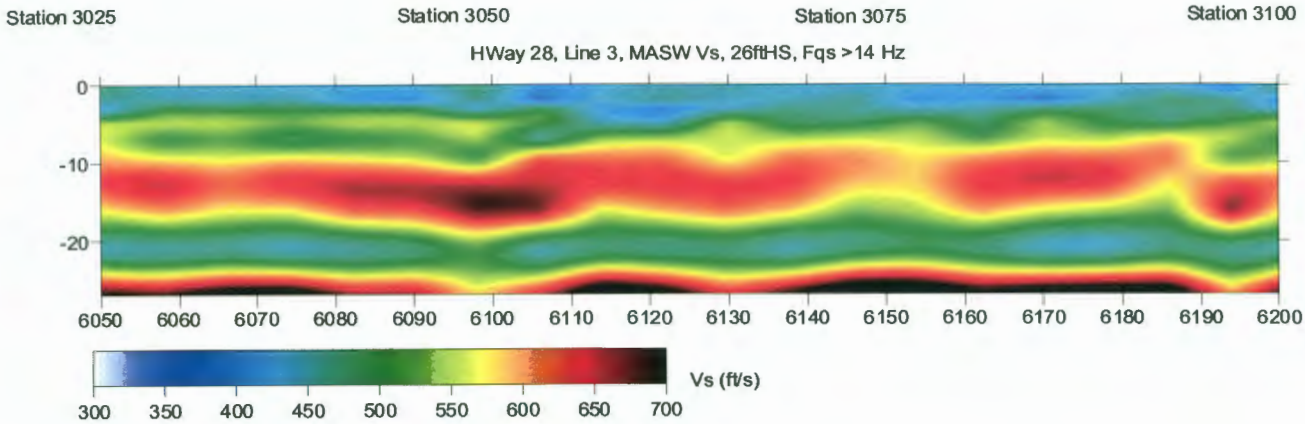



Figure 23. Shallow-focused MASW Vs results for Line 3.

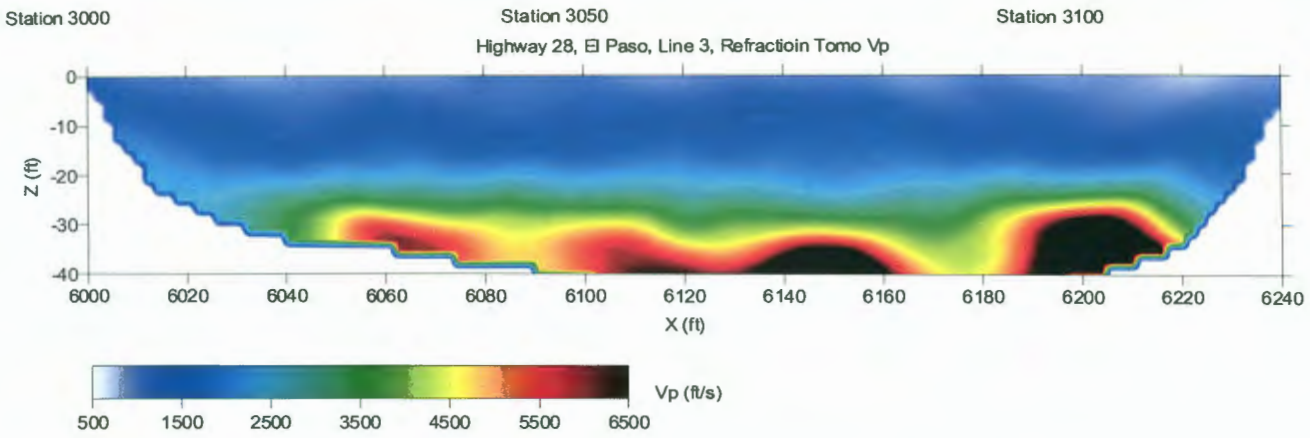



Figure 24. P-wave velocity model estimated for line 2 by analyzing P-wave-data first-arrival times using refraction-tomography software.

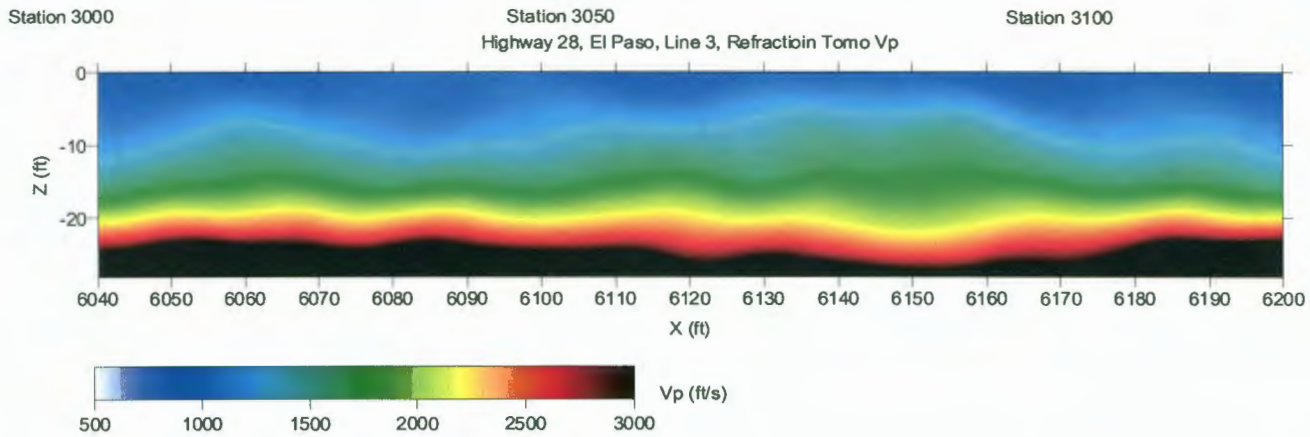



Figure 25. P-wave velocity model estimated for line 2 by analyzing P-wave-data first-arrival times using refraction-tomography software rescaled for comparison with the rest of the Vp and Vs results, focusing on the levee.

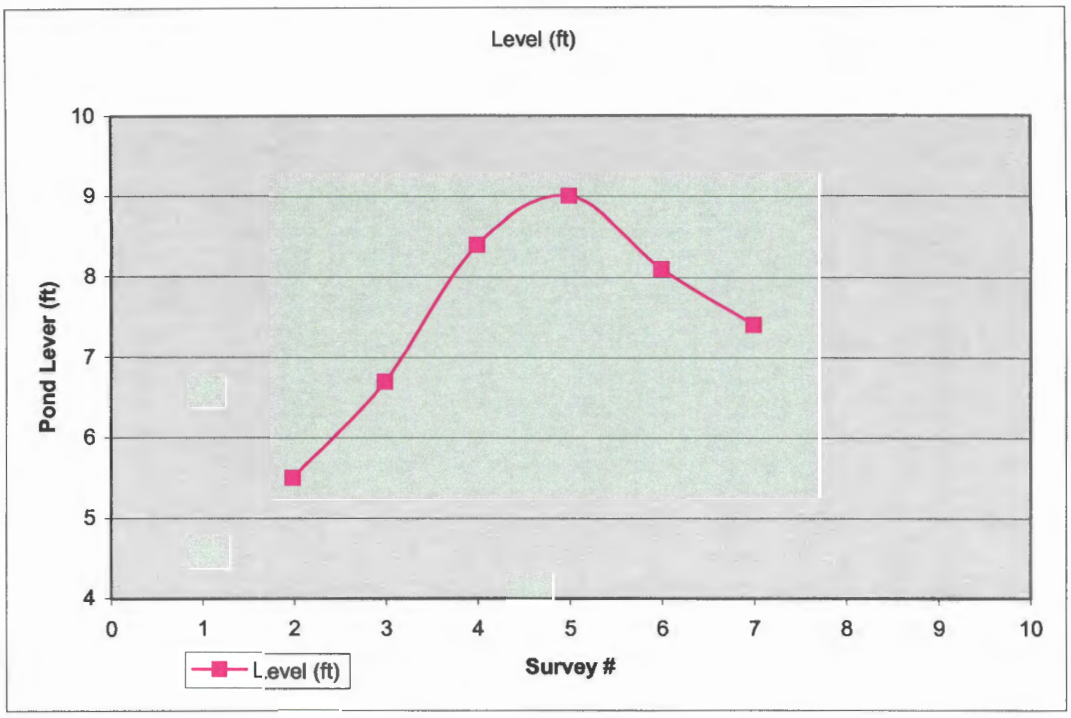



Figure 26. Water level for each of the surveys during the Ponding experiment at line 1.

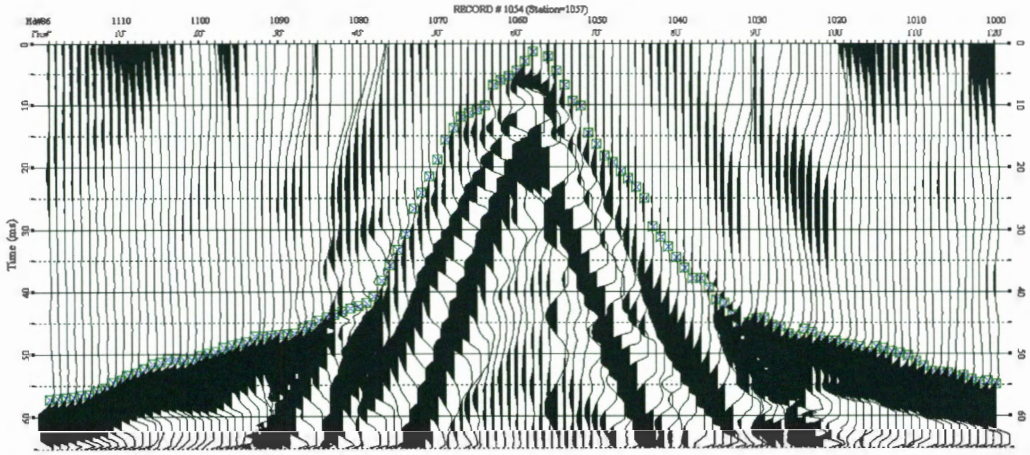



Figure 27. Estimation of first-arrival times on a P-wave seismic data with source located at station 1057 (horizontal location 2114 ft).

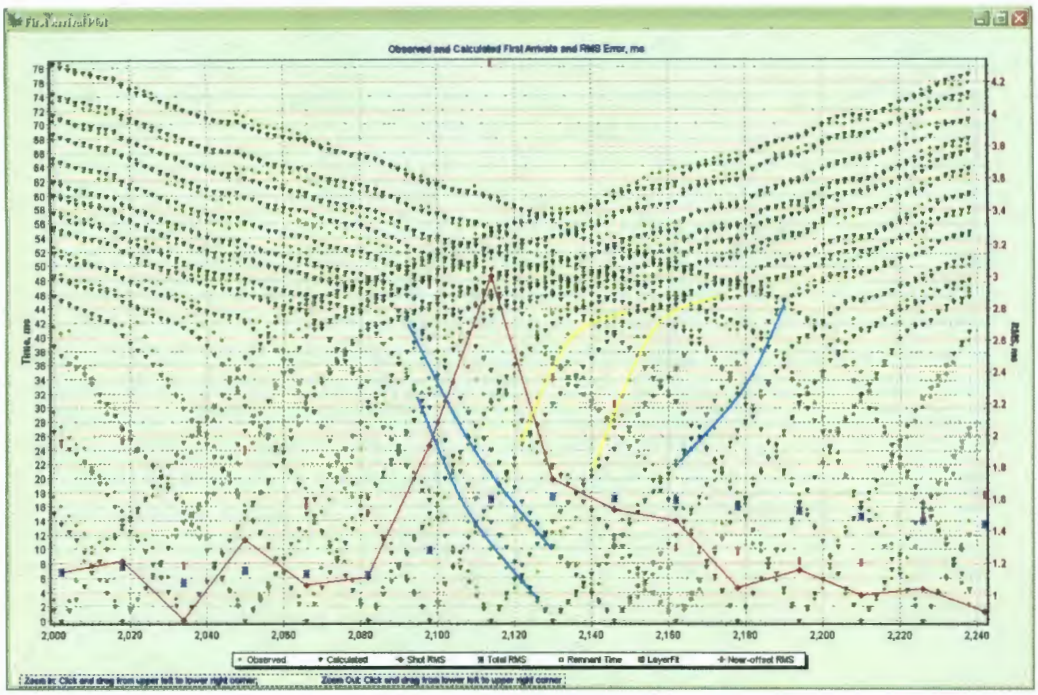



Figure 28. Misfit observations between the modeled (calculated) the observed first arrivals. Yellow lines indicate first arrivals that are greater than the modeled, blue lines indicated those that are smaller.

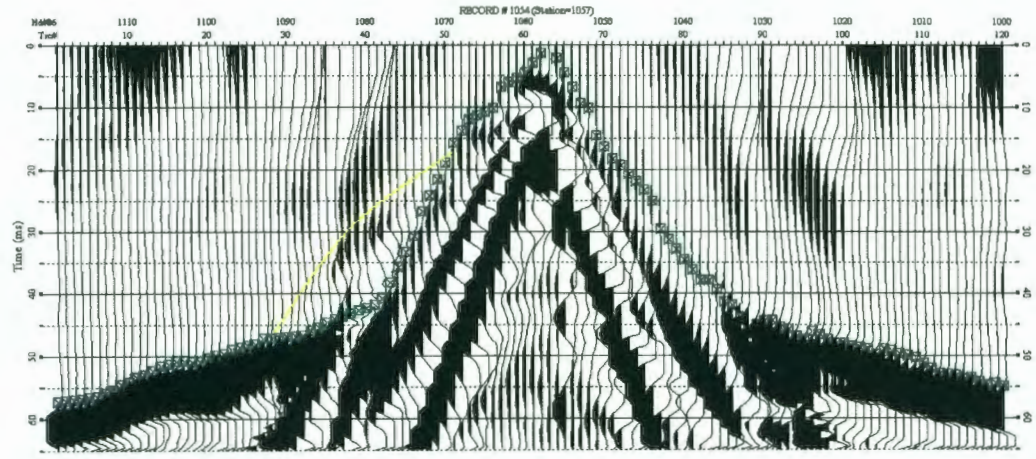



Figure 29. Estimation of first-arrival times on a P-wave seismic data with source located at station 1057 (horizontal location 2114 ft) and the model suggested first arrivals (yellow line).

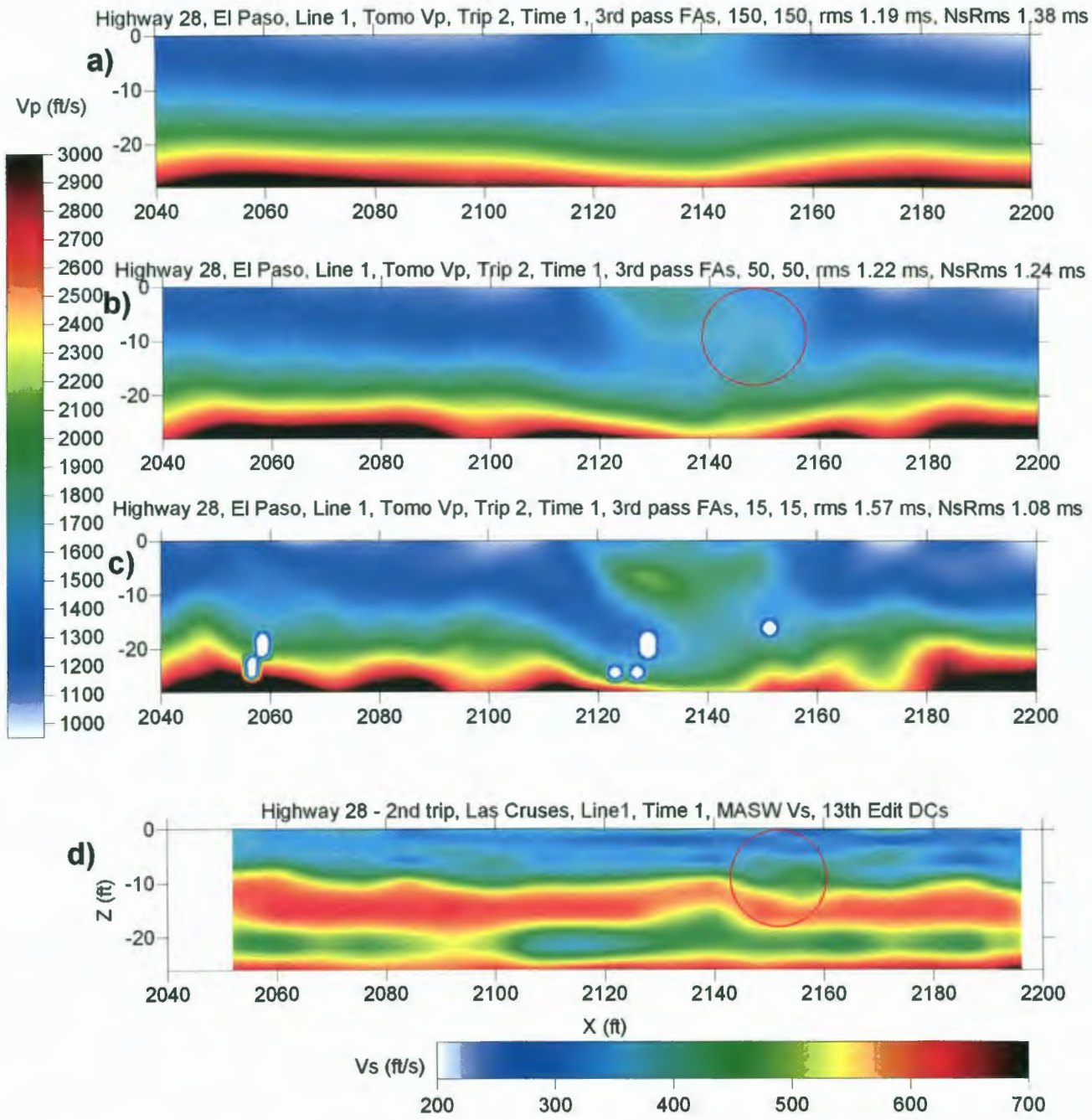



Figure 30. Highway 28, El Paso, Trip 2, Line 1, Vp refraction-tomography inversion regularization parameter (smoothing) testing and comparison with MASW Vs results. Red circles indicate areas with similarities between the Vs and Vp sections.

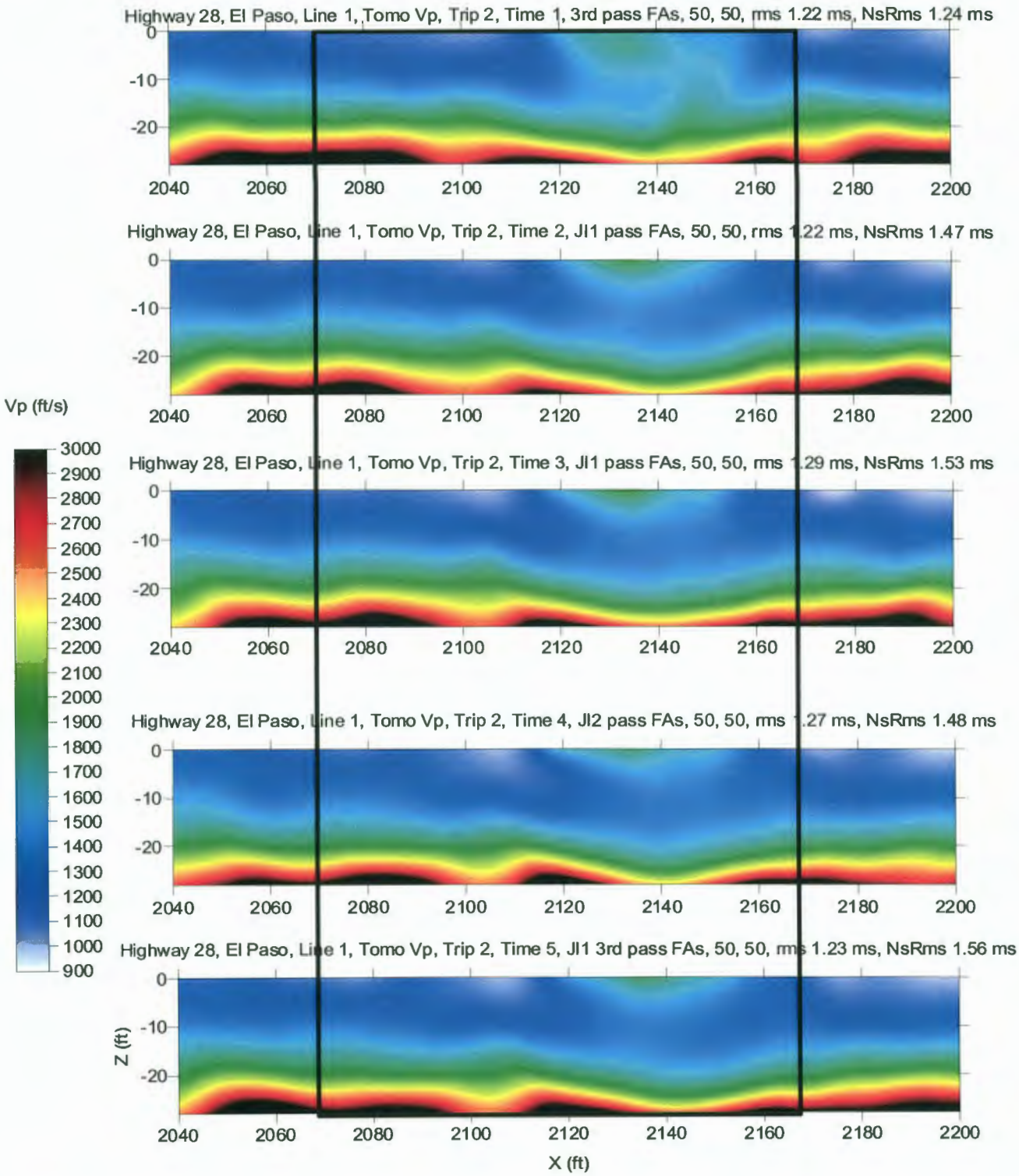



Figure 31. Refraction tomography Vp results at the top of the levee next to the pond for the first five time slices estimated at 4-hour intervals after the beginning of the test with the initial survey at the top and the fifth survey at the bottom of the display. The pond location is indicated by the thick lines.

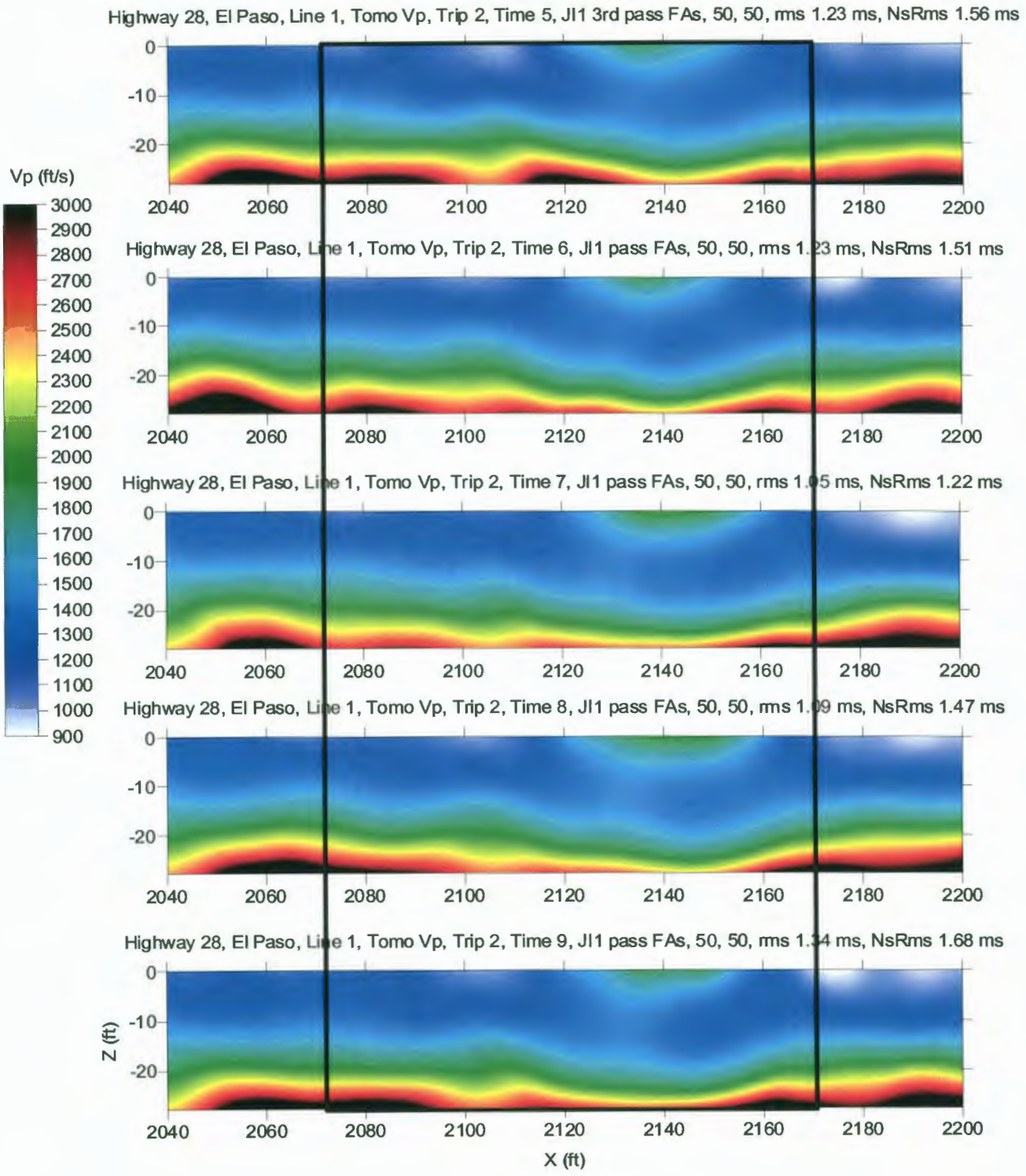



Figure 32. Refraction tomography Vp results at the top of the levee next to the pond for the last five time slices estimated at 4-hour intervals after the beginning of the test with the fifth survey at the top and the ninth survey at the bottom of the display. The pond location is indicated by the thick lines.

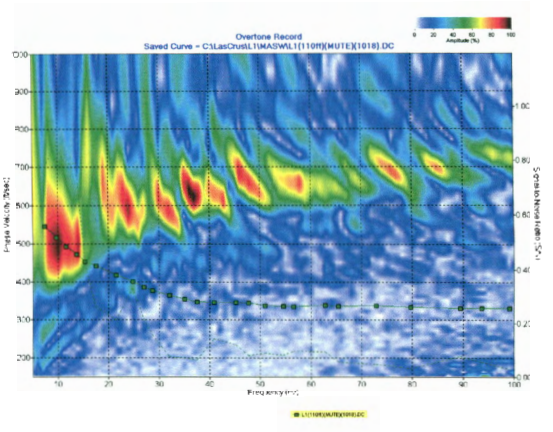



Figure 33. Rayleigh-wave dispersion curve analysis image of phase-velocity versus frequency domain.

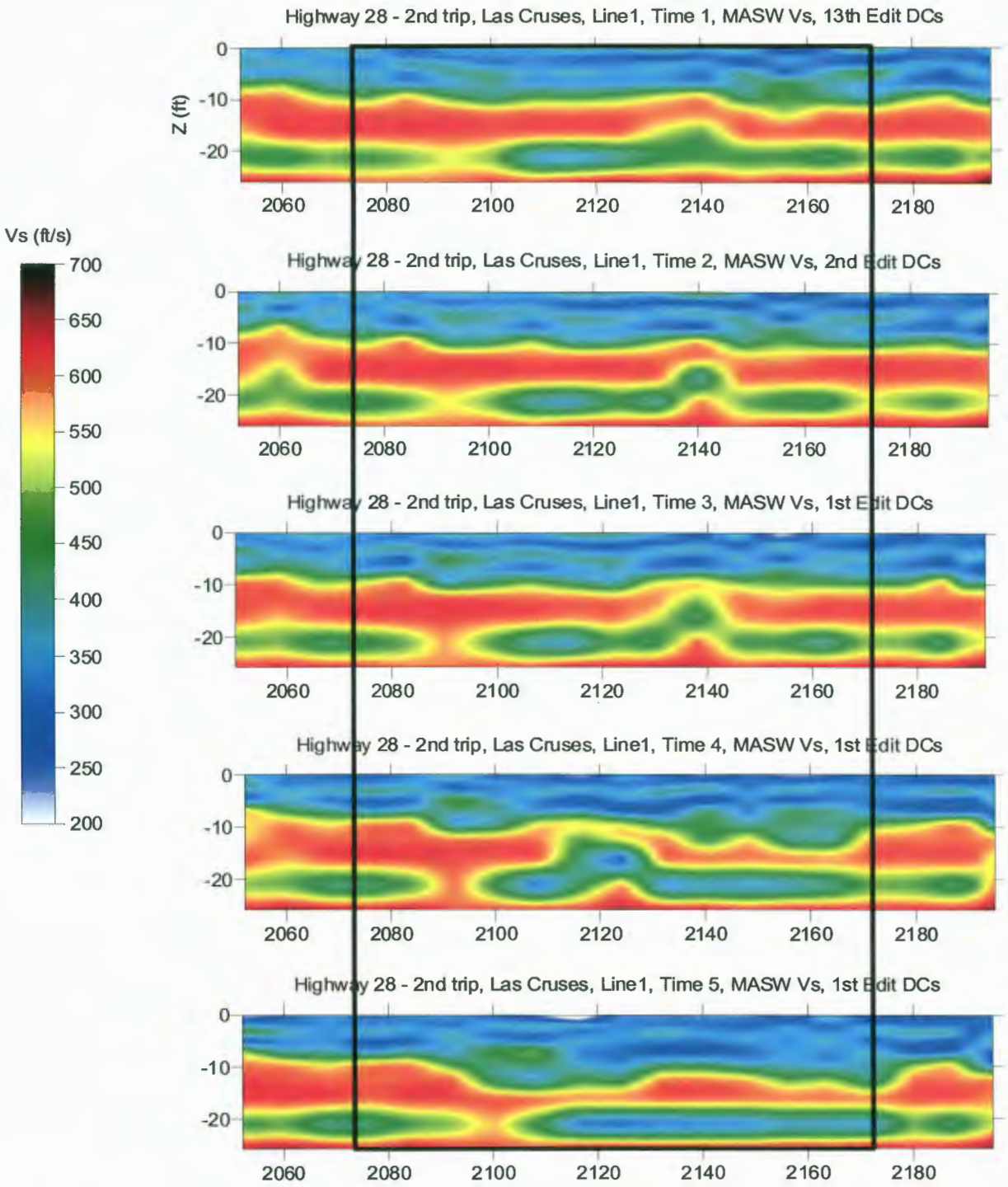



Figure 34. MASW Vs results at the top of the levee next to the pond for the first five time slices estimated at 4-hour intervals after the beginning of the test with the initial survey at the top and the fifth survey at the bottom of the display. The pond location is indicated by the thick lines.

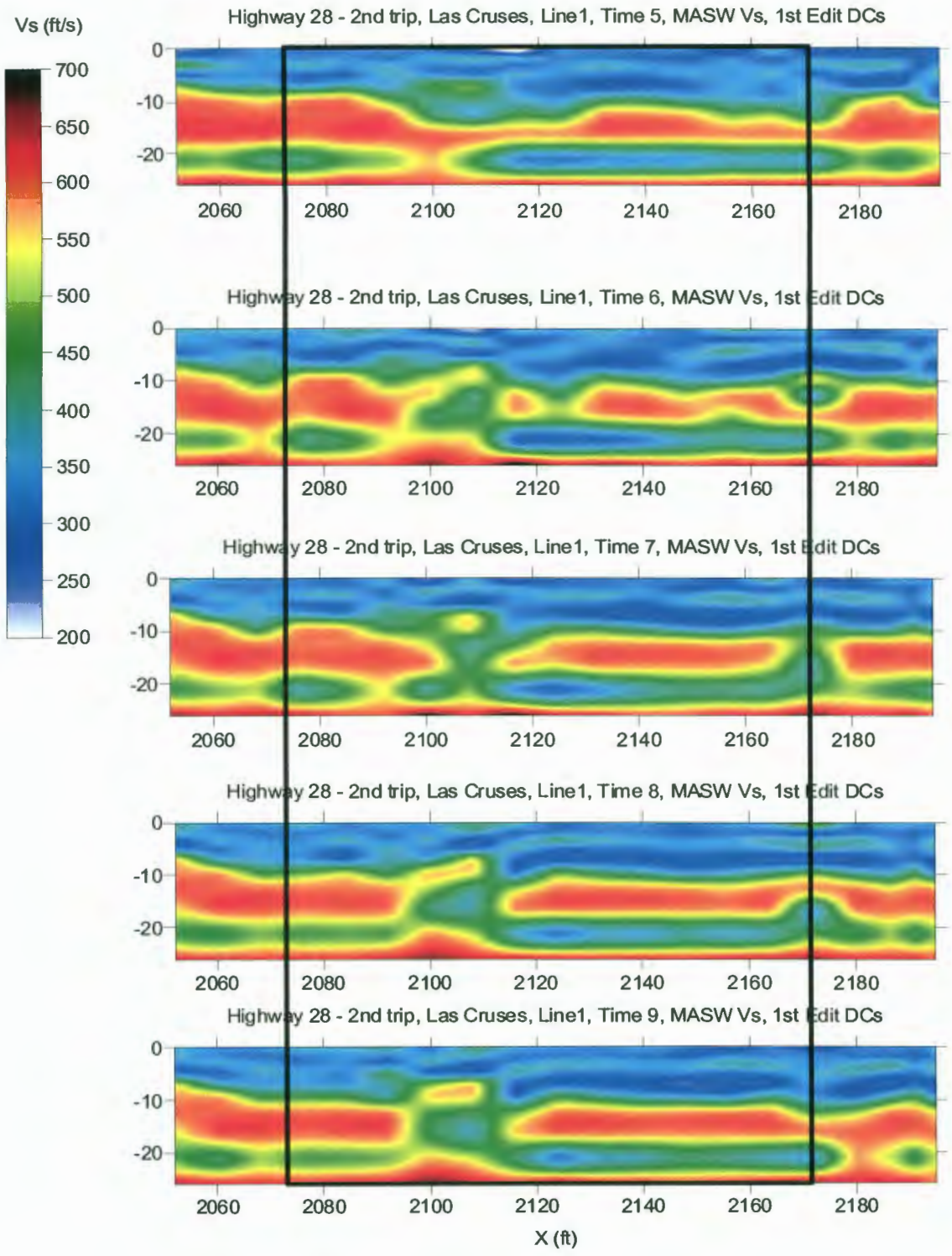



Figure 35. MASW Vs results at the top of the levee next to the pond for the last five time slices estimated at 4-hour intervals after the beginning of the test with the fifth survey at the top and the ninth survey at the bottom of the display. The pond location is indicated by the thick lines.

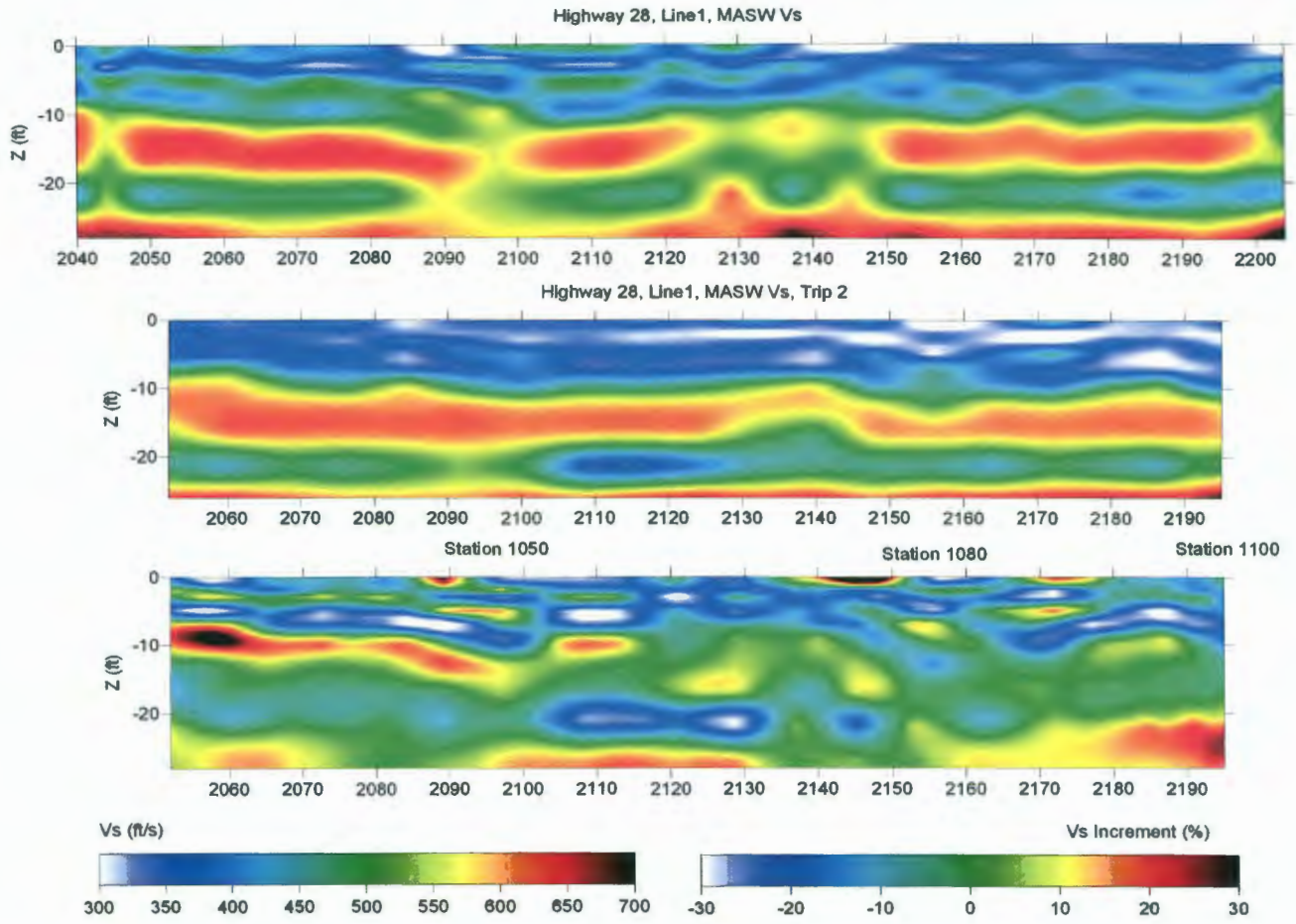



Figure 36. MASW 2D Vs results for Line 1, a) 2D Vs model obtained from the seismic data acquired during the first trip, b) 2D Vs model obtained from the seismic data acquired before the ponding experiment during the second trip, c) difference between the 2D Vs models obtained in the first and second trips.

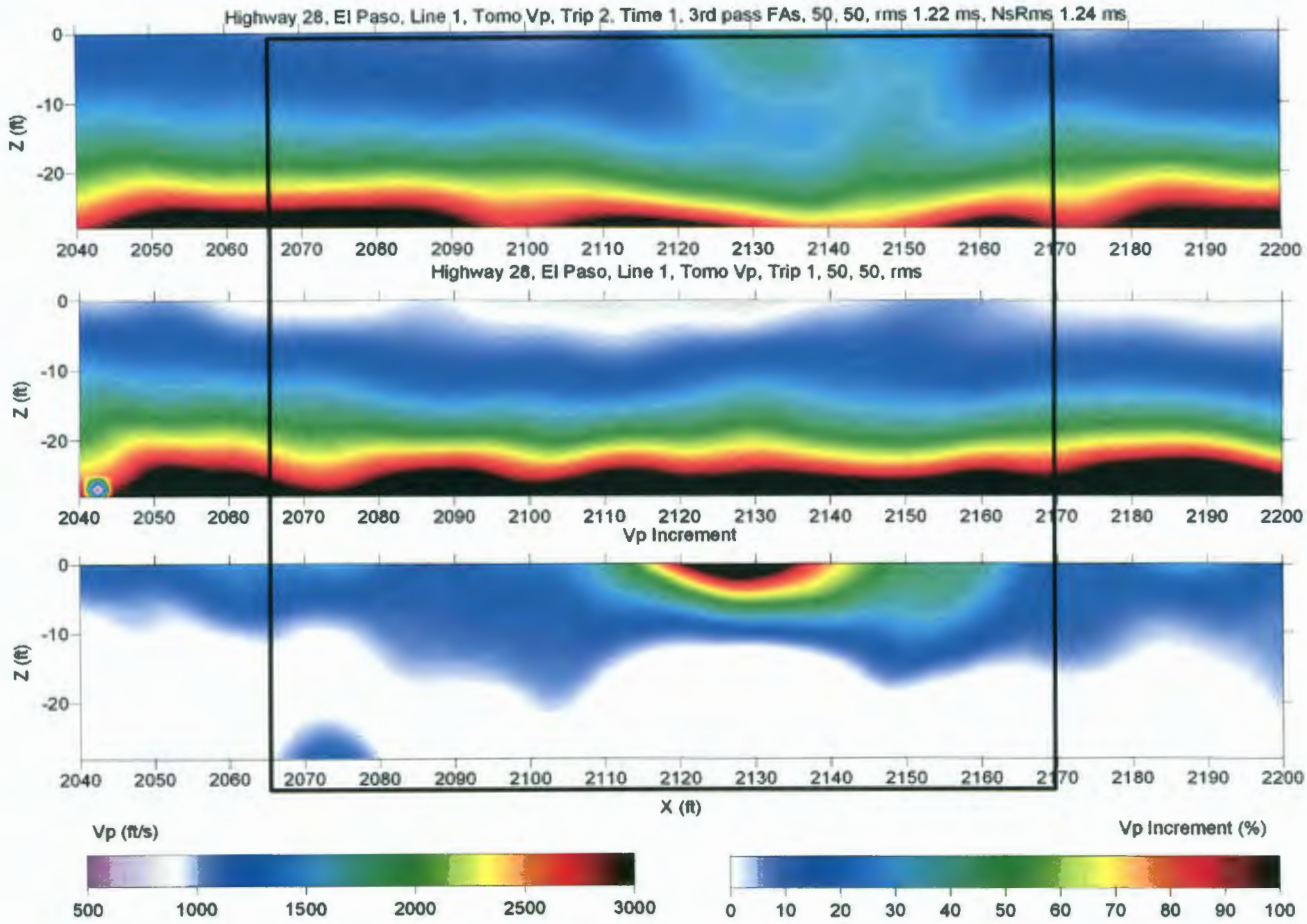



Figure 37. P-wave velocity model estimated for line 1 by analyzing P-wave-data first-arrival times using refraction-tomography software, a) P-wave velocity model obtained from the seismic data acquired during the first trip, b) P-wave velocity model obtained from the seismic data acquired before the ponding experiment during the second trip, c) difference between the P-wave velocity models obtained in the first and second trips.

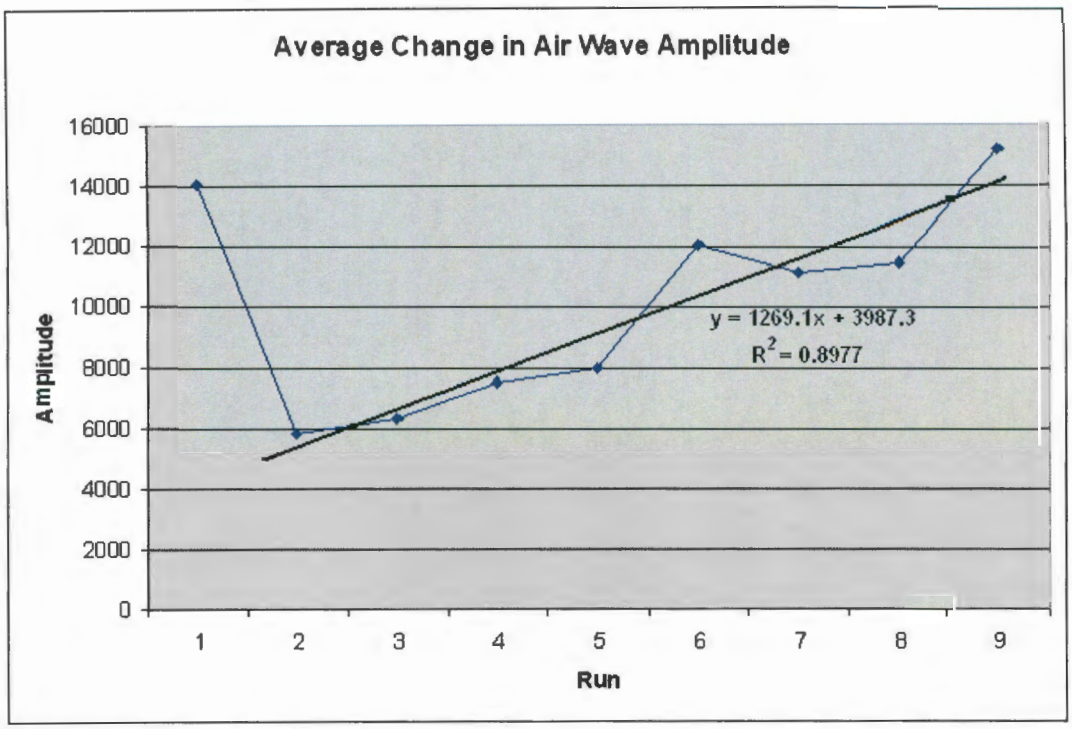



Figure 38. Average change in airwave amplitude.

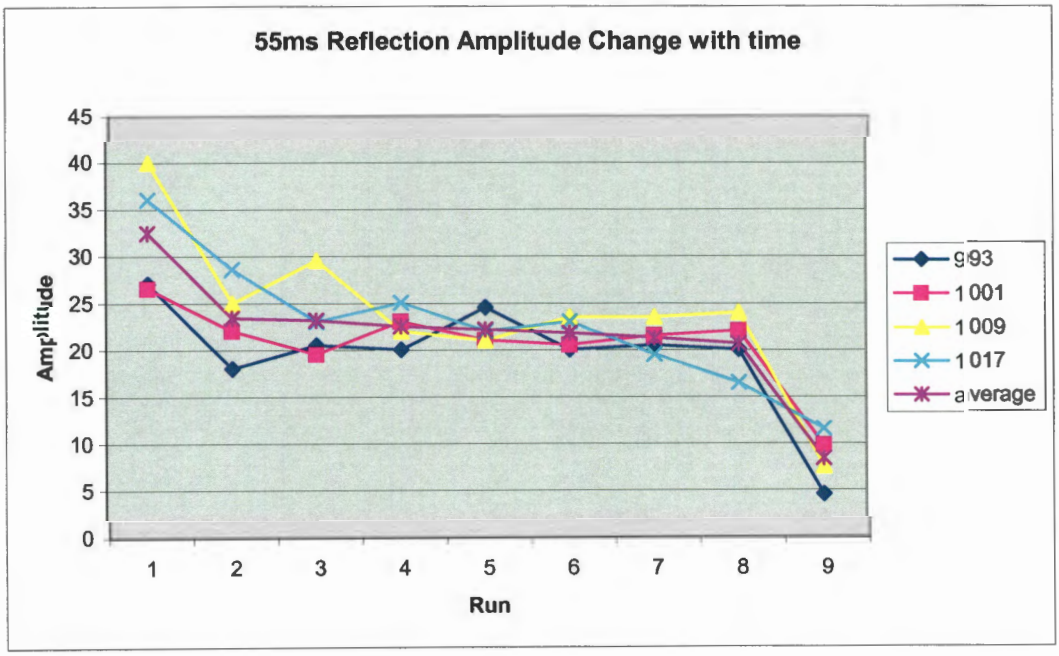



Figure 39. Change in reflection amplitude with time for the 55.0 ms reflection at the first four source stations

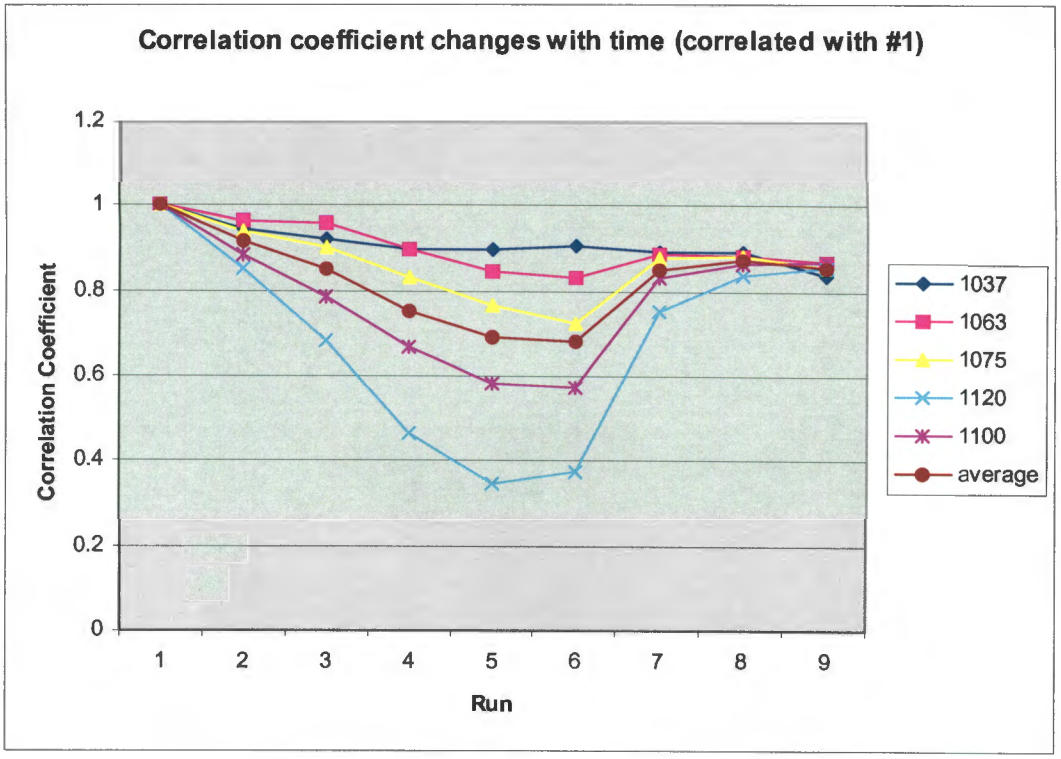



Figure 40. Correlation coefficient for wavelets correlated with that of run 1 for each run. These wavelets were taken from the same shot location, CMP 1017.

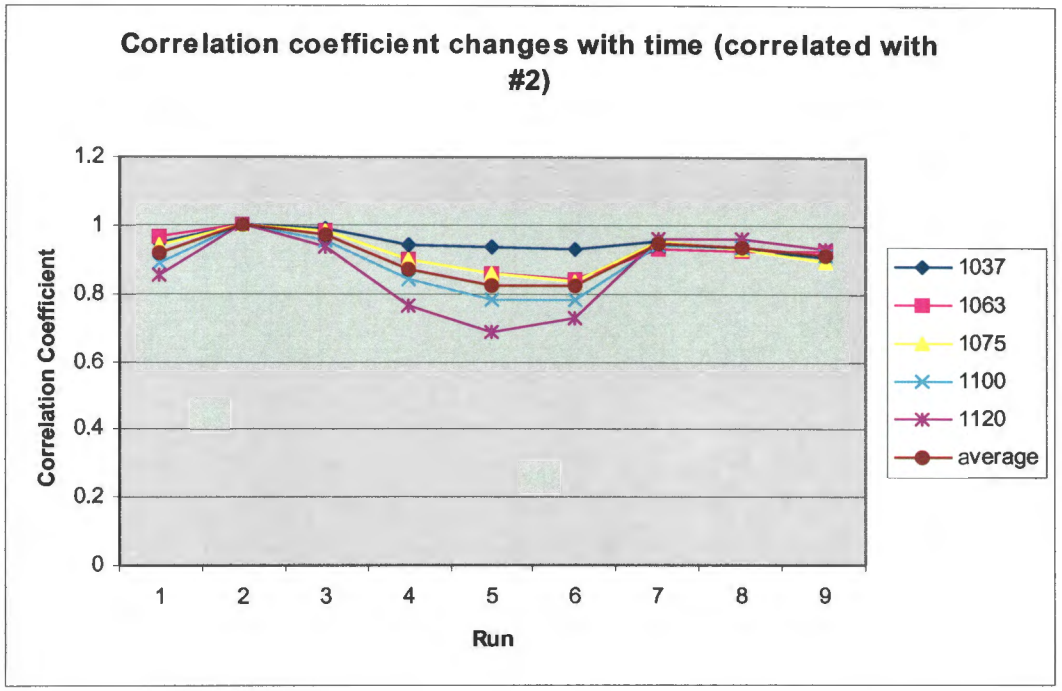



Figure 41. Same as Figure 40, except correlated with the wavelet from run 2, as opposed to 1.

# REFERENCES


Claerboat, J.F., 1992, Earth sounding analysis: processing versus inversion: Blackwell Science Publications.

Constable, S.C., R.L. Parker, and C.G. Constable, 1987, Occam's inversion: A practical algorithm for generating smooth models from electromagnetic sounding data: Geophysics, **52**, 289-300.

Hansen, C., 1998, Rank-deficient and discrete ill-posed problems. Numerical aspects of linear inversion: Department of Mathematical Modeling, Technical University of Denmark, Lyngby.

Ivanov, J., C.B. Park, R.D. Miller, and J. Xia, 2005, Analyzing and filtering surface-wave energy by muting shot gathers: Journal of Environmental and Engineering Geophysics, **10**, 307-321.

Menke, W., 1989, Geophysical data analysis: Discrete inverse theory: Academic Press, Inc.

Park, C.B., R.D. Miller, and J. Ivanov, 2002, Filtering Surface Waves: Proceedings of the Symposium on the Application of Geophysics to Engineering and Environmental Problems (SAGEEP 2002), Las Vegas, Nevada, February 10-14, 2002.

Tikhonov, A.N., and V.Y. Arsenin, 1977, Solutions of ill-posed problems: John Wiley and Sons.

Xia, J., C. Chen, G. Tian, R.D. Miller, and J. Ivanov, 2005, Resolution of high-frequency Rayleigh-wave data: Journal of Environmental and Engineering Geophysics, **10**, 99-110.